Contents lists available at ScienceDirect

Bioactive Materials

A deformable SIS/HA composite hydrogel coaxial scaffold promotes alveolar bone regeneration after tooth extraction

Shiqing Ma [a,1], Yumeng Li [b,1], Shiyu Yao [b,1], Yucheng Shang [b], Rui Li [b], Lijuan Ling [c], Wei Fu [a], Pengfei Wei [d,*], Bo Zhao [d,**], Xuesong Zhang [e,***], Jiayin Deng [b,****]

[a] Department of Stomatology, The Second Hospital of Tianjin Medical University, Tianjin, 300211, China
[b] School and Hospital of Stomatology, Tianjin Medical University, Tianjin, 300070, China
[c] Chinese People's Liberation Army General Hospital JingZhong MED Huangsi Out-patient department, Beijing, 100120, China
[d] Beijing Biosis Healing Biological Technology Co., Ltd, Beijing, 102600, China
[e] Department of Orthopaedics, The Fourth Medical Centre, Chinese PLA General Hospital, Beijing, 100048, China

ARTICLE INFO

ABSTRACT

After tooth extraction, alveolar bone absorbs unevenly, leading to soft tissue collapse, which hinders full regeneration. Bone loss makes it harder to do dental implants and repairs. Inspired by the biological architecture of bone, a deformable SIS/HA (Small intestinal submucosa/Hydroxyapatite) composite hydrogel coaxial scaffold was designed to maintain bone volume in the socket. The SIS/HA scaffold containing GL13K as the outer layer, mimicking compact bone, while SIS hydrogel loaded with bone marrow mesenchymal stem cells-derived exosomes (BMSCs-Exos) was utilized as the inner core of the scaffolds, which are like soft tissue in the skeleton. This coaxial scaffold exhibited a modulus of elasticity of 0.82 MPa, enabling it to adaptively fill extraction sockets and maintain an osteogenic space. Concurrently, the inner layer of this composite scaffold, enriched with BMSCs-Exos, promoted the proliferation and migration of human umbilical vein endothelial cells (HUVECs) and BMSCs into the scaffold interior ($\approx$3-fold to the control), up-regulated the expression of genes related to osteogenesis (BMP2, ALP, RUNX2, and OPN) and angiogenesis (HIF-1α and VEGF). This induced new blood vessels and bone growth within the scaffold, addressing the issue of low bone formation rates at the center of defects. GL13K was released by approximately 40.87 ± 4.37 % within the first three days, exerting a localized antibacterial effect and further promoting vascularization and new bone formation in peripheral regions. This design aims to achieve an all-around and efficient bone restoration effect in the extraction socket using coaxial scaffolds through a dual internal and external mechanism.

1. Introduction

During alveolar socket healing, the expression and interactions of different types of cells and several growth factors in the body are regulated spatially and temporarily to promote the remodeling and building of the alveolar socket [1]. Nevertheless, the alveolar bone, which is a tooth-dependent structure, is absorbed to varying degrees horizontally or vertically during physiological or pathological bone remodeling following tooth loss, due to a lack of functional stimulation and insufficient vascular blood supply [2]. Secondly, following tooth extraction, soft tissue cells can proliferate rapidly to the defective area of the extraction socket, thereby occupying the space necessary for bone tissue formation [3,4]. Due to the above reasons, natural healing of the alveolar socket following tooth extraction often fails to achieve complete regeneration of the alveolar bone, thereby affecting subsequent denture restoration [5]. To solve this problem, alveolar ridge

preservation (ARP) is a treatment performed instantly after complete tooth extraction to reduce the dimensional changes of the alveolar ridge, using a biomaterial filler with or without socket sealing [6–8]. Biological materials used for ARP include autogenous bone, allografts, and xenografts [9,10]. Currently, the extensively applied bone graft material in clinical practice is the xenograft Bio-Oss Collagen, where 10 % collagen serves as a binder to aggregate the dispersed Bio-Oss particles, enabling Bio-Oss Collagen to maintain bone formation space and guide bone regeneration when implanted into defects. However, considering the new bone quality of alveolar bone regeneration and the shortened healing time of the alveolar socket, Bio-Oss Collagen still lacks the necessary bioactive components [11,12]. Therefore, the development of multifunctional biomaterials for alveolar bone regeneration has become a research focus [13,14].

Scaffolds constructed from inorganic minerals and collagen promote the repair of alveolar bone defects and have shown positive results in clinical practice [15,16]. Small intestinal submucosa (SIS), an extracellular matrix material, boasts an abundance of natural collagen and numerous bioactive factors, imparting it with exceptional biocompatibility and the capability to dynamically and continuously facilitate tissue repair[17–19]. Self-assembly is an intrinsic property of collagen [20, 21]. Collagen molecules, which maintain their intact triple-helical structure in SIS collagen solution, can spontaneously and orderly assemble into three-dimensional SIS hydrogels through various inter- and intramolecular non-covalent interactions under the influence of pH value and temperature [22]. Based on this, SIS/HA scaffolds can be fabricated by incorporating hydroxyapatite particles with osteoconductive properties into SIS hydrogels [23]. The integration of HA with collagen effectively balances the high mechanical strength of the inorganic component with the characteristic flexibility of the organic component [24,25]. During alveolar bone regeneration, scaffold materials need provide reliable mechanical support to adapt to the dynamic physical microenvironment, maintain the porous structure of the osteogenic bone to achieve effective cellular infiltration, thereby enhancing the transduction of cellular mechanical signals for regeneration and differentiation [26]. In addition, the deformability of scaffold materials is also crucial. The deformable scaffold material easily conforms to the bone defect, reducing the gap between the scaffold and the surrounding tissue and limiting the micromotions of the scaffold material [27,28]. Although the SIS/HA scaffold provides mechanical support for bone regeneration, its plasticity remains relatively low, rendering it difficult to flexibly fill bone defects after tooth extraction. This emphasizes the significance of the scaffold structural design. Human bone possesses a distinctive composite structure, characterized by a rigid exterior and a hollow interior that houses soft components like bone marrow and blood vessels [29]. Inspired by the biomimetic bone structure, the exterior SIS/HA scaffold serves a pivotal supportive role, while the inner part of the scaffold is designed as a hollow structure to give space for deformation. Meanwhile, the SIS hydrogel was precisely injected into the hollow interior of the scaffold, serving as its inner core. By skillfully leveraging the pliability of hydrogels, the coaxial scaffold of SIS/HA composite hydrogels exhibits an excellent shaping ability, while maintaining good mechanical strength.

Cell homing is a crucial process for tissue repair, which attracts endogenous stem cells from the host to the defect site, eliminating the need for acquiring cells *in vitro* and achieving in situ bone regeneration in the alveolar socket [30]. Exosomes (Exos), which are nanometer-sized extracellular vesicles enriched with various bioactive factors, share similar functions with their parent cells and have gradually emerged as a potential strategy for bone tissue repair [31,32]. As a cell-free therapy, Exos recognize specific surface proteins of target cells, are internalized through endocytosis, phagocytosis, plasma membrane fusion, and other means, activate signaling pathways of recipient cells, modulate gene transcription and expression of target proteins to exert biological effects [33]. In the field of bone regeneration research, BMSCs-Exos have been widely applied [34]. Zhang et al. [35] demonstrated that BMSCs-Exos

can effectively activate the BMP-2/Smad1/RUNX2 and HIF-1α/VEGF signaling pathways, further enhancing the proliferation and migration of osteoblasts and human umbilical vein endothelial cells (HUVECs) towards bone defect, thereby triggering osteogenic and angiogenic processes. In most cases, the scaffold material is implanted within the bone defect, and bone tissue reconstruction predominantly progresses from the defect's periphery towards its center, with less osteogenesis at the center of the defect, which may be attributed to restricted cell migration and proliferation into the scaffold [36,37]. To address this challenge, the incorporation of active ingredients capable of driving endogenous stem cells into the hydrogel inside the scaffold aims to attract and promote the migration of BMSCs and HUVECs to the interior of the scaffold. The SIS hydrogel, which is filled inside the SIS/HA scaffold, is a highly efficient carrier for BMSCs-Exos, ensuring the stable and long-term release of exosomes in local regions, thereby fostering angiogenesis and osteogenic differentiation processes within the scaffold, and improving the efficiency of bone formation in the central area of the defect [38].

The oral cavity is a complex dynamic micro-ecosystem that is in direct contact with the external environment and harbors a diverse microbial community [39]. The human oral cavity is second only to the gut in the diversity of its microbiota, which is either attached to the surfaces of oral structures as plaque biofilms or resides in saliva, of which bacteria predominate [40]. Given the complexity of the oral environment, it is of paramount importance to prevent infection caused by scaffold implantation. To avoid this issue, cationic antimicrobial peptides (AMPs) have emerged as promising alternatives due to their broad-spectrum antimicrobial activity and less susceptibility to drug resistance [41,42]. GL13K (GKIIKLKASLKLL-CONH2), a cationic antibacterial peptide comprising 13 amino acids, is derived from human parotid gland secretory protein. The positively charged lysine residues in the peptide electrostatically attract the negatively charged bacterial membrane, destroying the bacterial membrane to achieve the antibacterial effect [43]. It has been reported that GL13K exerts inhibitory effects on common bacteria, including *Staphylococcus aureus*(*S.aureus*)and *Escherichia coli*, and also demonstrates excellent antibacterial effects on *Porphyromonas gingivalis* and *Streptococcus gordonii*, which are commonly found in the oral environment [44,45]. Moreover, GL13K has been observed to facilitate the proliferation, adhesion, and differentiation of HUVECs and BMSCs, up-regulate the expression of genes and proteins related to osteogenesis and angiogenesis, and promote angiogenesis and osteogenic differentiation [46,47]. Hence, loading the SIS/HA scaffolds with the antimicrobial peptide GL13K, which is rapidly released at the initial stage, exerts a local antimicrobial effect and creates a favorable environment for subsequent bone formation. Meanwhile, the release of GL13K in the periphery of the scaffold further recruits cells to the defective area, fostering vascularization and promoting new bone formation in the surrounding tissues. In addition, BMSCs-Exos wrapped in hydrogel inside the coaxial scaffold effectively and long-term promote the proliferation and migration of HUVECs and BMSCs into the scaffold, enhancing angiogenesis and osteogenic differentiation within the construct. This achieves a comprehensive effect, promoting bone repair from the outside to the inside and in all directions.

In our study, a coaxial SIS/HA composite hydrogel scaffold has been constructed, comprising an outer layer of SIS/HA scaffold loaded with GL13K and an inner core of SIS hydrogel loaded with BMSCs-Exos. Experiments *in vitro* and *in vivo* will be conducted to evaluate the cell compatibility, antibacterial properties, and osteogenic and angiogenic capabilities of the scaffold, hoping to provide a meaningful reference for the clinical treatment of alveolar bone regeneration.

2. Materials and methods

2.1. Preparation of SIS hydrogel

The process of obtaining small intestinal submucosa involved

mechanical scraping of the mucosa and serosal muscle layer, followed by washing with deionized water 3–5 times. Subsequently, the material was degreased for 12 h using a mixture of methanol and chloroform (v/v = 1:1), digested with 0.05 % trypsin/0.05 % EDTA for 12 h, treated with detergent (0.5 % sodium dodecyl sulfate in 0.9 % sodium chloride) for 4 h, sterilized with 0.1 % peroxyacetic acid and 20 % ethanol for 30 min, and finally dried and chopped at room temperature. The SIS (1 g) was immersed in 100 mL of 0.5 mol/L acetic acid solution, and 50 mg of pepsin was added for enzymatic hydrolysis, with stirring for 48 h. Following centrifugation, an acidic SIS pre-gel (10 % w/v) was obtained. The pre-gel was neutralized with a sodium hydroxide solution and incubated at 37 °C for 30 min in order to obtain the SIS hydrogel.

2.2. Collection and characterization of BMSCs-Exos

2.2.1. Isolation and purification of Exos

Bone marrow mesenchymal stem cells were cultured in dishes containing DMEM, 10 % Exos-free fetal bovine serum, and 1 % penicillin and streptomycin at 37 °C in a 5 % CO_2 atmosphere. Exosomes were isolated from the supernatant by removing cell fragments and centrifuging at 4 °C for 30 min at 1000 g and 60 min at 12000 g. The supernatant was then filtered through a 0.22 μm filter (Solarbio, China) and the precipitate was obtained by centrifugation at 100,000 g for 90 min. Subsequently, the precipitate was washed with PBS, after which Exos were obtained by centrifugation at 100,000 g for 1 h.

2.2.2. Identification and characterization of Exos

The morphology of exosomes was observed by transmission electron microscopy (TEM, Hitachi, HT7700, Japan). The particle size and distribution of exosomes were analyzed using nanoparticle tracking analysis (NAT, Nanosight NS300, UK). The markers of exosomes were identified through Western blot analysis, with cytochrome C serving as a negative control.

2.2.3. Internalization assay of Exos

The Exos that had been centrifuged were labeled with DiI (Beyotime, China). To investigate the uptake of BMSCs-derived Exos by BMSCs and HUVECs, the labeled Exos were incubated with BMSCs and HUVECs for 24 and 48 h, respectively. The cells were then washed with PBS and fixed in 4 % paraformaldehyde (Solarbio, China) for 30 min. After that, the cells were permeabilized with 0.5 % Triton X-100 (Solarbio, China) for 10 min and washed again with PBS. Finally, the nuclei were stained with DAPI solution (Solarbio, Beijing, China). Images were captured using a laser confocal scanning microscope (CLSM, LSM800, Zeiss, Germany). The cells were co-cultured with the G-SIS/HA + gel-Exos scaffold extracts. The uptake of DiI labeled BMSCs-Exos by BMSCs and HUVECs was observed after 1 and 3 days, respectively. Images were acquired using CLSM.

2.3. Preparation of SIS hydrogel with BMSCs-Exos

The neutral SIS pre-gel was combined with a solution of Exos (3.29 × 10^8 particles/mL) at 4 °C to prepare the SIS pre-gel loaded with Exos. To confirm the presence of Exos in the hydrogel, CLSM was used to observe Exos labeled with DiI. The hydrogel without Exos was used as a negative control.

2.4. Preparation of coaxial composite scaffold

2.4.1. Assembly of GL13K-SIS/HA scaffolds and SIS hydrogel-Exos

Hollow SIS/HA scaffolds were prepared using a template casting method. HA particles were stirred into the SIS hydrogel to form a mixture at low temperature, poured into a custom-made tubular mould, and freeze-dried completely to obtain the hollow SIS/HA scaffold (SIS: HA = 1:9). To make a GL13K solution with a concentration of 1 mg/mL, GL13K was dissolved in deionized water. The SIS/HA scaffolds were

immersed in the GL13K solution for 30 min, washed three times with PBS, and then ventilated and dried at room temperature to obtain the GL13K-loaded hollow SIS/HA scaffolds. The neutral SIS pre-gel loaded with Exos was uniformly filled into the hollow part of the SIS/HA scaffold by a syringe and placed at 37 °C for 30 min, resulting in the formation of a coaxial scaffold comprising a GL13K-loaded SIS/HA scaffold as the outer shell and SIS hydrogel containing Exos as the inner core.

2.4.2. Characterization of coaxial composite scaffold

To verify the characterization of the SIS/HA + gel coaxial scaffold, we used the Bio-Oss® Collagen, SIS/HA scaffold and SIS hydrogel as controls. The morphology of the SIS/HA scaffold, SIS gel, SIS/HA + gel scaffold, G-SIS/HA + gel-Exos and Bio-Oss® Collagen scaffold was observed using a scanning electron microscope (SEM, ZEISS, Germany) and Micro-CT (SkyScan 1276, Germany). Compression tests were performed on each scaffold using a mechanical testing machine (3367, Instron, USA) with a verification rate of 10 mm min^{-1}. The scaffolds were ground into a fine powder, and spectra ranging from 500 to 4000 cm^{-1} were collected using a Fourier transform infrared spectrometer (FTIR) (Nicolet iS50, Thermo Fisher Scientific, USA) to identify the chemical groups present in the samples. The porosity of each scaffold was calculated using the formula: Porosity(%)=$(V_0-V_e)/(V_t-V_e)$ × 100 %. Here, V_0 represented the initial ethanol volume, V_t represented the total volume after immersing the scaffold in ethanol for 2 min, and V_e represented the ethanol volume after removal of the scaffold. The scaffolds were freeze-dried and weighed to determine the initial weight (M_0) before being immersed in simulated body fluid (SBF). The samples were placed in a constant temperature oscillation box at 37 °C for 7, 14, 21, 28, 35, and 42 days. At each time point, the post-degradation weight (M_1) was determined by drying the samples. The degradation rate of the scaffold was calculated using the following formula: Degradation (%) = $(M_0-M_1)/M_0$ × 100 %.

2.4.3. Release of peptides and Exos on the coaxial composite scaffold

Different concentrations (500 μg/mL and 1000 μg/mL) of GL13K-SIS/HA + gel scaffolds were prepared and subsequently placed into well plates, with 1 mL of PBS added to each well. Following this, the entire well plate was positioned on a constant temperature shaker set at 37 °C. From day 1 up to day 30 (with sampling conducted every two days on days 1, 3, 5, …, and 30), 600 μL of release solution was collected and replaced with an additional 600 μL of PBS. The absorbance values of the GL13K solutions were measured using a microplate reader, and the GL13K release amounts of each sample were calculated by comparing them with a pre-established standard curve. The SIS/HA + gel-Exos coaxial scaffold and SIS gel loaded with Exos were incubated in PBS at 37 °C for 30 days, and the cumulative exosome release was calculated using the BCA protein detection kit (Solarbio, China).

2.5. Cell experiments in vitro

2.5.1. Cell proliferation and viability test

The Bio-Oss® Collagen, SIS/HA + gel, G-SIS/HA + gel, SIS/HA + gel-Exos, and G-SIS/HA + gel-Exos scaffolds were placed in sterile centrifuge tubes containing 10 mL of Dulbecco's modified Eagle's medium (DMEM) respectively and shaken slowly at 120 rpm in a 37 °C shaker. The supernatant was collected at specific time points according to experimental requirements and sterilized using a 0.22 μm filter membrane. Serum (10 %) and penicillin/streptomycin (1 %) were added to obtain sample extracts. Cell proliferation was assessed using the CCK-8 kit (Solarbio, China). BMSCs and HUVECs (6 × 10^3 cells/well) were seeded in 96-well plates and cultured with extracts from scaffolds (Bio-Oss® Collagen, SIS/HA + gel, G-SIS/HA + gel, SIS/HA + gel-Exos, G-SIS/HA + gel-Exos). The blank control group was cultured with complete medium. The absorbance (OD) values at 450 nm were measured using a microplate reader (Multiskan FC, Thermo Fisher Scientific, USA)

after 1, 3, 5, and 7 days of culture. To evaluate the cytotoxicity of the scaffolds, BMSCs, and HUVECs were co-cultured with sample extracts for 1 and 3 days. The cells were stained with an AO/EB kit (Sangon Biotech, China), and cell viability was observed. Images were taken using a fluorescence microscope (Olympus, Tokyo, Japan).

2.5.2. Cell migration assay

The migration ability of different groups of cells was detected using the Transwell assay. BMSCs and HUVECs (1×10^4 cells) were seeded in the upper chamber, while the lower chamber contained a sample extract (2 % FBS). After 24 h, the medium was discarded and fixed with 4 % paraformaldehyde for 30 min. Non-migrating cells were gently wiped with a cotton swab after 20 min of staining with 0.1 % crystal violet (Solarbio, China). Images were captured using light microscopy and analyzed with Image J software. The scratch assay was employed to investigate the impact of scaffolds from different groups on the horizontal migration capabilities of BMSCs and HUVECs. Initially, cells (2×10^5 cells/well) were seeded into 6-well plates separately. Once the confluency reached 100 %, a cell-free band was formed by vertical scratching with a 200 μL pipette tip. Following the scratch, sample extracts were added to the corresponding wells. The status of the scratch wound was observed using an inverted microscope at 0 h and 24 h post-scratch. ImageJ software was utilized to quantify the changes in the scratch area.

2.5.3. Cytoskeleton staining

To visualize the cytoskeleton of the different groups, BMSCs, and HUVECs were seeded in 24-well plates (1×10^4 cells/well) and co-cultured with sample extracts for 24 h. After fixation with 4 % paraformaldehyde for 30 min, the cells were permeabilized with 0.5 % Triton X-100 for 10 min. Actin filaments were stained with rhodamine B-phalloidin (Cytoskeleton, Inc., USA), and nuclei were stained with DAPI (Solarbio, China). The cytoskeleton was observed and images were captured using CLSM.

2.5.4. Tube formation assay

The tube formation experiments *in vitro* were conducted using ECMatrix Gel (Corning, 356234, USA). Matrigel was melted at 4 °C, and 60 μL was aspirated and injected into a 96-well plate, which was left at 37 °C for 30 min to solidify. Then, 3×10^4 HUVECs were inoculated onto the gel in the well plates and incubated for 6 h with the addition of sample extracts. The tube-forming effect was observed by light microscopy and analyzed using ImageJ software.

2.5.5. Alkaline phosphatase staining (ALP) and alizarin red staining (ARS)

BMSCs were inoculated at a concentration of 2×10^4 cells per well in a 24-well plate. Once the cells reached 70%–80 % confluency, the DMEM was replaced with osteogenic induction medium consisting of DMEM, 10 % FBS, 1 % penicillin and streptomycin, 50 μM ascorbic acid, 100 nM dexamethasone, and 10 mM β-glycerophosphate. After 7 and 14 days of culture with extracts from scaffolds, the cells in each group were stained with the BCIP/NBT alkaline phosphatase color development kit (Beyotime, China). For ARS staining, each group was stained with alizarin red solution (pH 4.2, Solarbio, China) for 20 min after 14 and 21 days of culture with extracts from scaffolds. The stained samples were gently rinsed with ddH$_2$O and observed under a light microscope to take pictures.

2.5.6. Quantitative real-time polymerase chain reaction(qPCR)

The study detected the expression of genes related to osteogenesis and angiogenesis using qPCR. The HUVECs were cultured with extracts from scaffolds for three days, while the BMSCs were cultured in osteogenic induction medium and sample extracts for 14 days. Total RNA was extracted using Trizol reagent (Invitrogen, USA), followed by cDNA synthesis using GoScript Reverse Transcription Mix (Promega, USA). The qPCR analysis was performed with SYBR Green Master Mix and the

Roche LC480II system (Roche, Switzerland). The $2^{-\Delta\Delta Ct}$ method was used to analyze gene expression, with GAPDH serving as a reference gene to normalize the expression of target genes. The primer sequences were designed by Sangon Biotech, China.

2.5.7. Western blotting assay

HUVECs were harvested after 3 days of culture with extracts from scaffolds. BMSCs were harvested 14 days after induction of osteogenesis. Protein extracts were diluted with protein loading buffer (5X, NCMBiotech, China). The extracts were then separated using 10 % sodium dodecyl sulfate (SDS)-polyacrylamide gel electrophoresis (Solarbio, China) and transferred to a polyvinylidene difluoride (PVDF) membrane (Sigma, USA) at 300 mA for 100 min. The PVDF membranes were subsequently blocked with 5 % bovine serum albumin (BSA, Solarbio, China) for 1 h. Following this, they were incubated overnight at 4 °C with primary antibodies, namely anti-BMP2, anti-ALP, anti-OPN, anti-RUNX2, anti-VEGF, anti-HIF-1α, and anti-GAPDH. Finally, the membranes were incubated with secondary antibodies conjugated with horseradish peroxidase (HRP) (1:1000, Beyotime, China) at room temperature for 2 h. The antibody-bound proteins were detected using an enhanced chemiluminescence (ECL) Western blotting analysis system (New Cell & Molecular, China). Band analysis was performed using Image J software, and all values were normalized to GAPDH values.

2.5.8. Immunofluorescence staining

Cellular immunofluorescence staining was employed to observe the expression of osteogenic and angiogenic proteins. 1×10^4 BMSCs and HUVECs were cultured in 24-well plates with sample extracts. After 3 days of cell culture, cells were fixed with 4 % paraformaldehyde for 30 min and permeabilized with 0.5 % Triton X-100 for 20 min, rinsed with PBS, and then treated with BSA (5 mg/mL) solution for 30 min. Primary antibodies such as ALP, BMP2, RUNX2, VEGF, and HIF-1α were incubated overnight at 4 °C with the cells. Cells were then incubated with Cy3-conjugated antirabbit secondary antibody (1:1000, Abcam, UK) for 1 h under light-free conditions. Cell nuclei were stained with DAPI (Solarbio, China) solution. Images were captured using CLSM.

2.6. Antibacterial experiment in vitro

2.6.1. Preparation of bacteria

S. aureus and *Streptococcus sanguis (S. sanguis)* were inoculated in LB liquid medium, while *Fusobacterium nucleatum (F.nucleatum)* was inoculated in BHI liquid medium, and then incubated at 37 °C for 24 h. Subsequently, the concentration of each bacterial solution was adjusted to 10^6 CFU/mL by dilution with liquid medium for future use.

2.6.2. Morphology of bacteria

The morphology of the bacteria on the surface of the scaffolds was examined using SEM. The scaffolds were co-cultured with 2 mL of bacterial solution in 24-well plates at 37 °C for 24 h. After that, the scaffolds were gently washed with sterile PBS and fixed in 2.5 % glutaraldehyde at 4 °C overnight. After being fixed, the scaffolds underwent gradient dehydration treatment by being placed successively in 30 %, 40 %, 50 %, 60 %, 70 %, 80 %, 90 %, and 100 % ethanol solutions for 10 min each. Subsequently, the scaffolds were dried and coated with gold before being observed under SEM.

2.6.3. Plate colony count

The scaffolds were immersed in 2 mL of bacterial solution and co-cultured at 37 °C for 24 h. Subsequently, 1 mL of the bacterial solution was aspirated and diluted 10^3-10^5 times with liquid medium. Then, 100 μL of *S. aureus* and *S. sanguis* bacterial solution was taken and spread on LB solid medium plates, while 100 μL of *F. nucleatum* bacterial solution was spread inside CDC anaerobic blood agar plates. Bacterial colonies on the plates were observed after 24 h, and pictures were taken with a camera. The colonies were then counted using Image J software.

2.6.4. Live/dead bacterial staining

The viability of the bacteria was assessed using a Live/Dead staining kit (Life Technologies Corporation, CA). A volume of 2 mL of the bacterial solution was aspirated into the 24-well plate, followed by co-culture with each group of scaffold materials at 37 °C for 24 h. The bacterial solution was then discarded and replaced with the working solution for staining. Dead (red) and live (green) bacteria were observed by CLSM.

2.6.5. Inhibition zone experiment

LB solid medium plates and CDC anaerobic blood agar plates were prepared. 100 μL of a diluted solution containing *S. aureus* and *S. sanguis* bacteria was spread evenly on the LB solid medium plate, while a solution containing *F. nucleatum* bacteria was spread on the CDC anaerobic blood agar plate. Subsequently, the sterilized scaffolds were placed on the plates and incubated for 24 h at 37 °C. Photographs were taken, and the diameter of the inhibition zone was measured.

2.7. Bone regeneration in vivo

2.7.1. Rat alveolar bone defect model

The experiment was approved by the Animal Ethics and Welfare Committee of Tianjin Medical University. A rat alveolar bone defect model was used to evaluate the bone regeneration potential of the co-axial scaffold. This experiment adopted the male Sprague-Dawley (SD) rats, which were randomly divided into six groups: Blank, SIS/HA + gel, G-SIS/HA + gel, SIS/HA + gel-Exos, G-SIS/HA + gel-Exos and Bio-Oss® Collagen. Following anesthesia of the rats by inhalation of isoflurane, the gingiva of the rats was gently separated with a dental probe, and then the crown was clamped by a vascular clamp. The right maxillary first molar was extracted and irrigated with saline. The scaffold was then placed into the extraction socket, and the alveolar socket without the scaffold served as a blank control. Finally, cyanoacrylate adhesive was used to seal the mucosal tissue around the wound. Three days following the implantation of scaffolds, rats were sacrificed and the presence of bacterial infection at the implantation site was examined by plate colony counting. Under continuous inhalation anesthesia with isoflurane, G-SIS/HA + gel-Exos scaffold materials were implanted into the tooth extraction sockets of rats (n = 3 in each group). BMSCs-Exos were labeled with DiR, and GL13K was labeled with Rhodamine B. Images were captured using IVIS at selected time points (3d, 7d, 14d, 21d, 28d) to evaluate the release of GL13K and BMSCs-Exos *in vivo*.

2.7.2. Micro-CT analysis

Rats were euthanized 1 month after surgery, and their maxillae were obtained and fixed in 4 % histiocyte fixative (Solarbio, China). The reconstructed maxillae were scanned using Micro-CT. The three-dimensional reconstructed images were viewed using CTvox software, and the new bone volume fraction (BV/TV), bone mineral density (BMD), and trabecular thickness (Tb. Th) at the defect site were analyzed using CTAn software. New bone formation in the defect area was viewed in the sagittal direction using Dataview software.

2.7.3. Histological and immunohistochemical staining

The maxillary specimens were decalcified with an EDTA decalcification solution (pH 7.2, Solarbio, China) for one month. Thereafter, they were dehydrated, embedded, and cut into thick sections. The specimens were then subjected to hematoxylin and eosin (HE) and Masson trichrome staining. For immunohistochemical staining, sections were incubated overnight at 4 °C with primary antibodies, including OCN and CD34, and then treated with secondary antibodies.

2.7.4. Subcutaneous scaffold implantation model

To observe the *in vivo* degradability of scaffolds, male Sprague-Dawley (SD) rats were used and randomly divided into five groups: Bio-Oss® Collagen, SIS/HA + gel, G-SIS/HA + gel, SIS/HA + gel-Exos, and G-SIS/HA + gel-Exos. The rats were anesthetized with isoflurane inhalation, and approximately 1 cm longitudinal incisions were made on both sides of the back of each rat to create subcutaneous pockets and place the sterile scaffolds. Four weeks post-implantation, the samples, as well as the hearts, livers, and kidneys, were harvested and fixed in 4 % paraformaldehyde, followed by H&E staining.

2.8. RNA sequencing and data analysis

BMSCs were seeded into a 6-well plate and subsequently incubated with different scaffold extracts at 37 °C for 14 days. Total RNA was extracted from the cells using TRIzol reagent and stored at −80 °C before sequencing. Sequencing analysis was performed by Novogene Biotech Co., Ltd. (Beijing, China). Rigorous quality control of the mRNA was conducted using an Agilent 2100 bioanalyzer, followed by PE150 sequencing on the Illumina platform. DESeq2 was applied to analyze differentially expressed genes (DEGs). The threshold for significant differential expression was set at $|\log2(\text{FoldChange})| \geq 1$ and $padj \leq 0.05$. Additionally, clusterProfiler software was used to conduct Gene Ontology (GO) functional enrichment analysis and Kyoto Encyclopedia of Genes and Genomes (KEGG) pathway enrichment analysis on the set of differential genes. A corrected *P-value < 0.05* indicated significant enrichment of the DEGs.

2.9. Statistical analysis

The study presented results as mean ± standard deviation, repeated at least three times. Data were statistically analyzed using one-way analysis of variance (ANOVA) and Tukey's test. P-values were considered statistically significant if they were less than 0.05 (*$P < 0.05$*), 0.01 (**$P < 0.01$*) and 0.001 (***$P < 0.001$*).

3. Results and discussion

3.1. Characterization of BMSCs-Exos

Exosomes are of great interest in the medical field as intercellular communication factors [48]. BMSCs-derived Exos were isolated from the culture medium of BMSCs by ultracentrifugation (Fig. 1A), and identified by TEM, NTA, and Western blot. TEM images showed that the Exos presented a cup-shaped or round-shaped morphology with a bilayer membrane structure (Fig. 1B). The average diameter of the extracted vesicles was 106.8 nm, as determined by NTA analysis (Fig. 1C and D), which was consistent with the range of exosome diameters (40–160 nm) [49]. Western blot analysis demonstrated the presence of exosome-specific protein markers (Alix, CD63, CD9) in the exosomes, while Cytochrome C, serving as a control, was observed only in the cells (Fig. 1E) [50]. These results collectively indicated the successful isolation of BMSCs-Exos. Subsequently, SIS gel-Exos was prepared by incorporating the isolated Exos into SIS hydrogel. Exosomes labeled with DiI in SIS hydrogel were observed by CLSM, exhibiting red fluorescence, thereby confirming the successful loading of Exos into SIS hydrogel (Fig. 1F). To observe the expression and location of Exos in BMSCs and HUVECs, it was demonstrated in the CLSM images that Exos were taken up by the cells distributed around the nucleus (blue, DAPI), and the number of Exos uptake by the cells incubated for 48 h was found to be higher than that at 24 h, indicating that Exos could be uptake into the cytoplasm (Fig. 1G and H).

To investigate the stability of exosomes in coaxial scaffolds, the scaffolds were placed in PBS and their exosome release was continuously collected for 30 days. The standard curve is presented in Figure S1A. The result demonstrated that, compared to the SIS hydrogel, the cumulative release profile of the SIS/HA + gel-Exos scaffold exhibited a continuous and slow release of exosomes. This was because exosome release from the SIS/HA + gel-Exos scaffold needed to pass through both the SIS gel and the SIS/HA bilayer structure (Fig. 1I). From day 11 onwards,
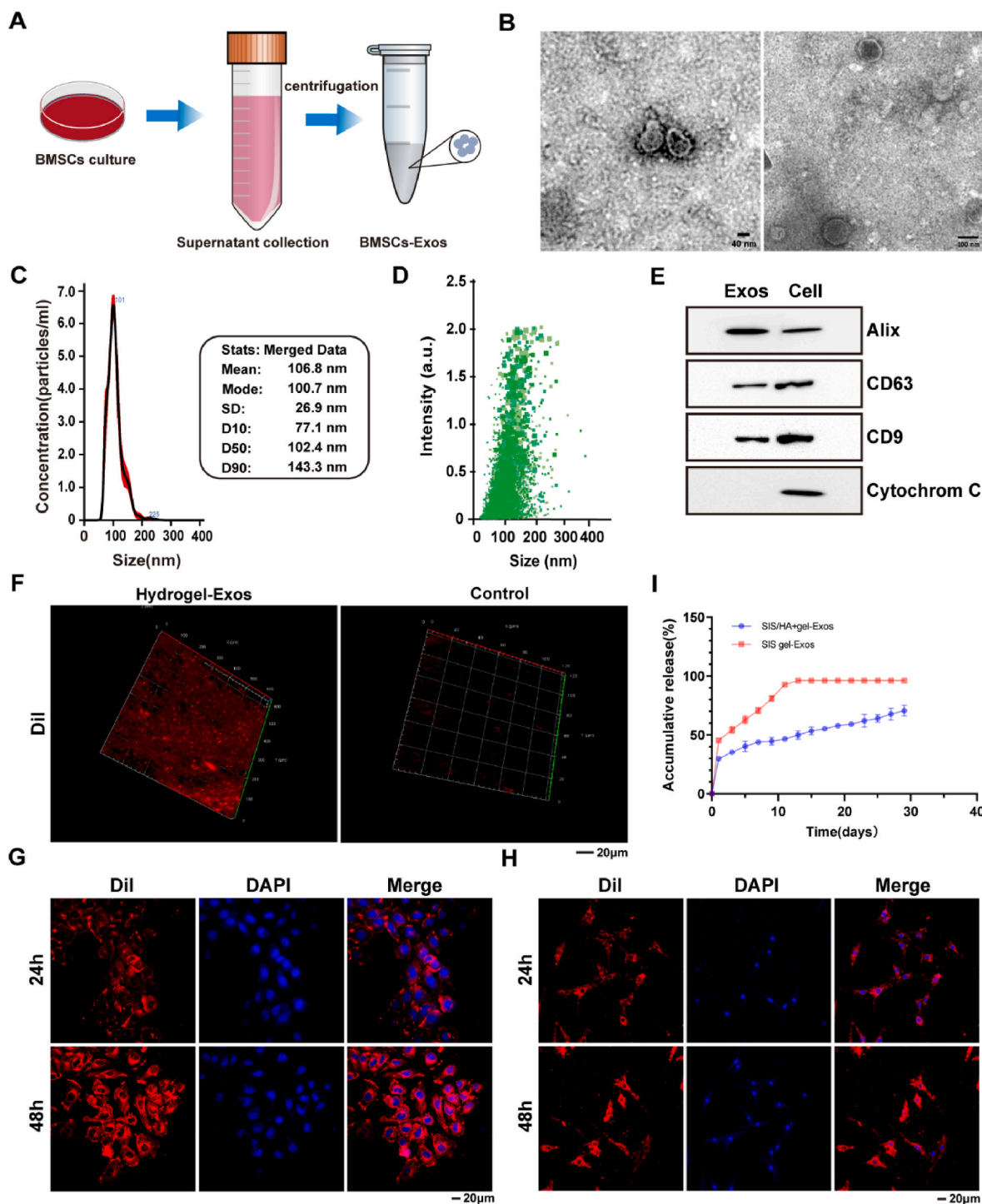
Fig. 1. Characterization of BMSCs-derived exosomes. (A) Schematic of exosome synthesis. (B)Representative TEM images of BMSCs-derived Exos. (C) NTA presented the size and particle concentration of BMSCs-Exos. (D) Distribution and intensity of Exos. (E) Western blot analysis of Alix, CD63, CD9, and Cytochrome C expression in BMSCs-derived Exos. (F) CLSM images of SIS hydrogels loaded with BMSCs-Exos. Exos were labeled with DiI. (G) Internalization of DiI-labeled Exos by HUVECs for 24 and 48h. (H)Internalization of DiI-labeled Exos by BMSCs for 24 and 48 h. Nuclei (blue); Exos (red). (I) Release curves of Exos in SIS gel-Exos and SIS/HA + gel-Exos scaffold.

exosome release in the SIS hydrogel approached a plateau, whereas the SIS/HA + gel-Exos scaffold showed a cumulative release of approximately 46.53 ± 0.947 % on day 11 and continued to release exosomes slowly over time. Therefore, the SIS/HA + gel-Exos scaffold was more effective in loading and sustaining the release of exosomes. We co-cultured G-SIS/HA + gel-Exos scaffold extracts with cells and observed the uptake of DiI-labeled BMSCs-Exos by BMSCs and HUVECs

after 1 day and 3 days. The CLSM images (Fig. S1. B) revealed that the exosomes (red, DiI) were taken up by the cells and distributed around the nuclei (blue, DAPI). Importantly, the number of Exos taken up by cells after 3 days of incubation was higher than that after 1 day, indicating that BMSC-Exos can be slowly released from the coaxial scaffold and efficiently taken up by the cells. To date, numerous studies have comprehensively highlighted the promising applications of Exos in the

fields of regenerative medicine and tissue repair due to their stability, biosafety, and multifunctionality. However, it is noteworthy that the bioavailability of free-form Exos in the target area is suboptimal, and the lack of an effective controlled release mechanism somewhat restricts their efficacy [51]. To address this issue, researchers have actively explored strategies for combining exosomes with various biomaterials,

including bioactive ceramics, hydrogels, and synthetic polymers [52, 53]. These integration strategies have not only effectively prolonged the storage duration of exosomes but also significantly improved their release characteristics, thereby successfully overcoming the limitations of native exosomes in practical applications. Consequently, these advancements have paved new avenues for the further application of
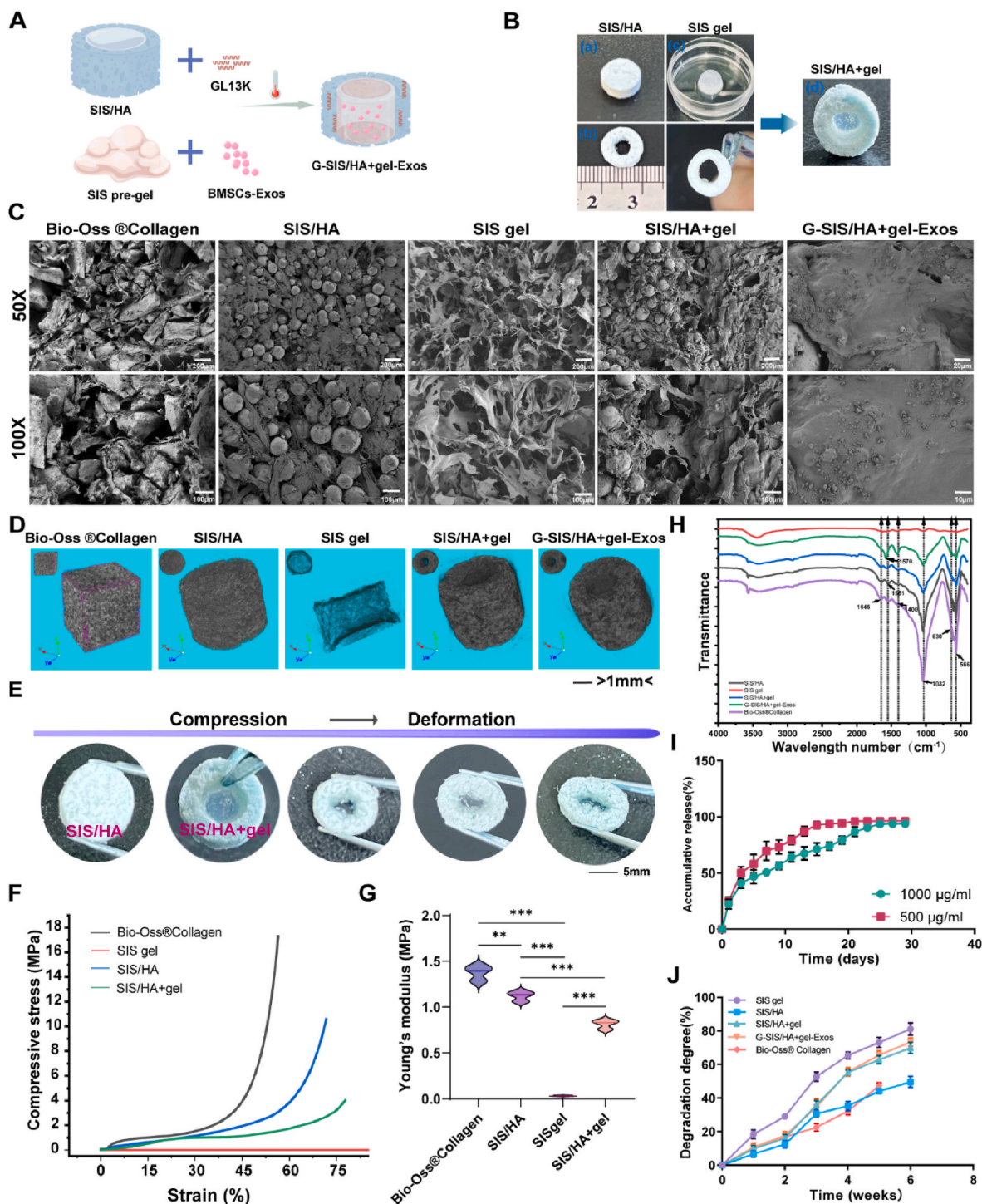

Fig. 2. Preparation and characterization of coaxial scaffolds. (A) Schematic of coaxial scaffold preparation. (B) Rough appearance of different scaffolds: (a) SIS/HA scaffold (b) Hollow SIS/HA scaffold (c) SIS gel (d) SIS/HA + gel scaffold. (C) SEM images of SIS/HA, SIS gel, SIS/HA + gel, Bio-Oss® Collagen, and G-SIS/HA + gel-Exos scaffolds. (D) Micro CT images of SIS/HA, SIS gel, SIS/HA + gel, Bio-Oss® Collagen, and G-SIS/HA + gel-Exos scaffolds. (E) Images of compression deformation of SIS/HA and SIS/HA + gel scaffolds. (F) Stress-strain curves of different scaffolds. (G) Young's moduli of the different scaffolds. (H) FTIR spectra of SIS/HA, SIS gel, SIS/HA + gel, Bio-Oss® Collagen, and G-SIS/HA + gel-Exos scaffolds. (I) Release profiles of GL13K coaxial scaffold. (J) Degradation curves of SIS/HA, SIS gel, SIS/ HA + gel, Bio-Oss® Collagen, and G-SIS/HA + gel-Exos scaffolds.

exosomes in the medical field [54,55].

3.2. Preparation and characterization of coaxial composite scaffolds

Fig. 2A presented the experimental schematic of the fabricated co-axial scaffolds. A general overview of the manufactured SIS/HA, SIS gel, and SIS/HA + gel composite scaffolds could be observed in Fig. 2B. The SIS/HA scaffold (a), boasting a diameter of 1 cm and a height of 5 mm, has a rough surface. To determine the optimal ratio of inner diameter to outer diameter for hollow scaffolds, we prepared hollow scaffolds with inner diameters of 3 mm, 5 mm, and 7 mm, respectively (with outer-to-inner diameter ratios of 1:3, 1:5, and 1:7), and subjected them to pressure compression tests. The experimental results indicated that while the scaffold with an outer-to-inner diameter ratio of 1:3 exhibited good mechanical strength, it lacked sufficient deformability; conversely, the scaffold with a ratio of 1:7 showed better deformation performance but compromised mechanical strength. In comparison, the scaffold with a ratio of 1:5 maintained high mechanical strength while also demonstrating a certain level of deformability. Therefore, we fabricated a hollow SIS/HA scaffold (b) with an outer diameter of 1 cm and an inner diameter of 5 mm (Figure S2A). The neutral SIS pre-gel exhibited a fluidic consistency, with a transparent to translucent appearance, while the SIS gel (c) could be formed following incubation at 37 °C for 30 min, displaying a flat and smooth surface and some elasticity. During this process, collagen molecules within SIS spontaneously and orderly assemble into SIS hydrogels under the influence of pH and temperature. The self-assembly process can be divided into two stages: nucleation and nuclear growth. During the nucleation stage, the N-terminus and C-terminus overlap, a process regulated by two terminal peptides; whereas fiber growth is achieved through lateral and longitudinal intermolecular interactions [56,57]. Compared to traditional collagen gels, SIS gel uniquely retains the bioactive factors present in the decellularized ECM. Leveraging this unique advantage of SIS, coaxial scaffolds have been successfully fabricated by injecting SIS pre-gel into the lumen (d) of hollow SIS/HA scaffolds. The surface morphology of different scaffolds was observed by SEM at different magnifications (Fig. 2C). Images of the Bio-Oss® Collagen scaffolds revealed large, irregular inorganic particles derived from calcined bovine bone, with collagen fibers wrapping around and binding these particles together. However, the images of the SIS/HA scaffolds showed that the HA particles were morphologically regular and uniformly distributed in the SIS collagen. The freeze-dried SIS gel exhibited an interconnected porous network structure. Furthermore, in the images of SIS/HA + gel, the hollow SIS/HA scaffolds were visible along with the SIS gel, where the SIS collagen interconnected at the interface, demonstrating the successful preparation of the coaxial scaffolds. Subsequently, the G-SIS/HA + gel-Exos scaffolds were observed to have numerous aggregated peptide particles, indicating effective loading of GL13K onto the coaxial scaffolds. Micro CT was further utilized to scan Bio-Oss® Collagen, SIS/HA, SIS gel, SIS/HA + gel, and G-SIS/HA + gel-Exos scaffolds (Fig. 2D). Three-dimensional images of different scaffolds were reconstructed from the perspectives of side and cross-section. The results indicated that the inorganic particles in Bio-Oss® Collagen were relatively large and of varied morphologies, with the excess spaces between particle forming the pore structure of the material. In the SIS/HA scaffolds, HA particles were tightly bound to collagen, with collagen serving as an adhesive to bond all particles into the scaffold, revealing an abundant pore structure. The SIS gel exhibited a complex interlaced structure of internal collagen fibers. Notably, uniform filling of the SIS gel was clearly observed in the hollow regions of the SIS/HA scaffolds.

In bone tissue engineering, the mechanical properties of scaffolds are an important feature [26]. The three-dimensional porous scaffold material placed in the tooth extraction socket should possess a certain mechanical strength to maintain the three-dimensional space for bone formation, while also having the deformability to easily fill the defect in the tooth extraction socket and create a beneficial biomimetic bone

environment. In Fig. 2E, the deformation of the scaffold was conspicuously discernible. Notably, the SIS/HA + gel scaffold underwent a significant deformation even under mild extrusion, standing in stark contrast to the relatively inflexible SIS/HA scaffold. This heightened deformation capacity of the SIS/HA + gel scaffold is primarily attributed to its distinctive hollow structure, which encapsulates the SIS gel within the scaffold, exhibiting remarkable compressibility. To explore the mechanical strength of the scaffold, the SIS/HA + gel scaffold was measured by mechanical performance test, with SIS/HA scaffold, Bio-Oss® Collagen, and SIS gel serving as controls. The stress-strain curves of different scaffolds were shown in Fig. 2F. The stress-strain curve of SIS gel tended to be linear, indicating that SIS gel had low mechanical strength and collapsed when under stress. The SIS/HA scaffold was prepared by incorporating HA particles into SIS gel. However, when the strain exceeded 60 %, the SIS/HA scaffold was gradually compacted, and while stress increased, the strain hardly changed. Therefore, the addition of HA significantly enhanced the mechanical strength of the scaffold, but the mechanical properties of the SIS/HA scaffold were slightly lower compared to Bio-Oss® Collagen. In contrast, as the stress on the SIS/HA + gel scaffold increased, the strain increased proportionally. When the strain exceeded 30 %, the stress-strain curve became flattened out, and the coaxial scaffold underwent plastic deformation until the strain exceeded 75 %, at which point the scaffold was gradually compacted. The results showed that the SIS/HA + gel scaffold exhibited significant advantages compared to the SIS/HA scaffold and SIS gel, as it possessed both good mechanical strength and a certain degree of deformability. Young's modulus was calculated as the slope of the linear region in the corresponding stress-strain curve (Fig. 2G). The experimental results showed that the commercial Bio-Oss® Collagen exhibited a high modulus of elasticity, indicating a stiff scaffold structure. The SIS/HA + gel scaffold, on the other hand, exhibited a delicate balance of properties, with an elastic modulus of 0.82 MPa, exactly between that of the SIS/HA scaffold and the SIS gel. This property was due to the ingenious combination of the SIS/HA scaffold and SIS gel, which allowed the SIS/HA + gel scaffold to retain the necessary mechanical strength, while at the same time providing the material with a degree of deformability. Research on the modulation of mesenchymal stem cell (MSC) differentiation by material elastic modulus/stiffness has garnered significant attention. It has been shown that poly(glycolide-co-sebacate) (PGS) materials exhibit properties that are closer to osteoid rather than mature natural bone, with an elastic modulus that falls within the "osteogenic induction" range (25–40 kPa), which has been proven effective in inducing stem cell differentiation towards the osteogenic lineage. This characteristic allows bone tissue to mature in an environmental matrix with mechanical properties that are more akin to those of osteogenic progenitor cells/stem cell differentiation, thereby developing into mature bone capable of bearing weight [58]. Notably, numerous studies have shown that MSCs exhibit more pronounced cell growth and osteogenic differentiation tendencies on materials with stiffnesses beyond this range. Hu et al. prepared demineralized bone matrix (DBM) scaffolds with varying stiffnesses (66.06 ± 27.83 MPa, 26.90 ± 13.16 MPa, and 0.67 ± 0.14 MPa). Compared to the first two stiffnesses, the DBM scaffold with a stiffness of 0.67 ± 0.14 MPa not only promoted osteogenesis but also significantly enhanced bone integration [59]. Chen et al., on the other hand, utilized three-dimensional printing technology to directly assemble porous bioactive glass nanoparticle scaffolds (BGNS) with polycitrate-siloxane (PCS), resulting in BGNS@PCS scaffolds that exhibited exceptional elasticity modulus (0.78 MPa) and compressive strength, significantly promoting cell proliferation and facilitating osteogenic differentiation of BMSCs [60]. Therefore, compared to high-stiffness matrices, low-stiffness biomaterials enhance cells' ability to perceive physical stimuli, thereby facilitating the transmission of mechanical signals to related proteins on target cell membranes, more effectively supporting cell proliferation, and enhancing osteogenic cell differentiation [61]. In view of this, the SIS/HA + gel scaffold, which has a modulus of elasticity of 0.82 MPa,

has the potential to enhance osteoblast differentiation by promoting osteogenic signaling more effectively through mechanical stimulation mechanisms. FTIR was used to characterize the related chemical groups of the Bio-Oss® Collagen, SIS/HA scaffold, SIS gel, SIS/HA + gel scaffold, and G-SIS/HA + gel-Exos scaffold. As evident from Fig. 2H, all scaffolds exhibited characteristic absorption bands associated with collagen. Specifically, the vibration exhibited at 1646 cm^{-1} (C=O) was associated with tensile vibration of the amide I band, the amide II band displayed N-H deformation at 1551 cm^{-1}, and the amide III band manifested N-H deformation at 1400 cm^{-1}. Furthermore, in the Bio-Oss® Collagen, SIS/HA scaffold, SIS/HA + gel scaffold, and G-SIS/HA + gel-Exos scaffold, characteristic peaks associated with HA were observed at 566 cm^{-1} (bending vibration peak of O-P-O), 603 cm^{-1} (bending vibration peak of PO$_4^{3-}$ group), and 1032 cm^{-1} (stretching vibration peak of PO$_4^{3-}$ group), confirming the successful integration of HA particles into the collagen. Additionally, the spectra of the G-SIS/HA + gel-Exos scaffold exhibited a characteristic peak at 1570 cm^{-1}, attributed to GL13K (amide II), thus validating the presence of GL13K in the coaxial scaffold. Intensive studies have indicated that scaffolds exhibiting porosity comparable to human trabecular bone (ranging from 70 % to 90 %) efficiently facilitate oxygen and nutrient transport, thereby encouraging the growth of bone tissue and vascularization within the scaffold structure [62,63]. As depicted in Figure S2B, the SIS gel exhibited a porosity of 85.09 ± 0.54 %, while the porosity of the SIS/HA scaffolds was lower, at 66.37 ± 1.02 %. The porosity of Bio-Oss® Collagen was 61.88 ± 3.33 %, which was not statistically significantly different from that of the SIS/HA scaffolds. The SIS/HA + gel scaffold exhibited a porosity of 75.38 ± 0.06 %, which fell between the two aforementioned scaffolds. Therefore, the SIS/HA + gel scaffold possessed an optimal porosity, making it a suitable candidate for bone tissue engineering applications.

According to relevant reports, GL13K, as a highly effective antibacterial agent, has demonstrated bactericidal activity against bacteria such as *Pseudomonas aeruginosa*, *Escherichia coli*, *Fusobacterium nucleatum*, and *Streptococcus gordonii*, with a minimum inhibitory concentration (MIC) below 100 μg/mL [64]. Further research has revealed that the functionality of GL13K extends beyond this, as it also promotes cell recruitment, modulates immune responses, and significantly enhances osteoblast differentiation and angiogenesis, exhibiting multifaceted biological activities. Zhang et al. innovatively constructed a sustained-release hydrogel system for GL13K peptide on micro-/nanostructured titanium surfaces. Experimental data showed that GL13K at a concentration of 200 μg/mL exhibited good sustained-release properties in this system, which significantly up-regulated the mRNA expression levels of osteoblast-related genes (e. g., OPG, ALP, OPN, and OCN) and effectively promoted osteoblast differentiation. Additionally, this sustained-release system effectively inhibited the growth of *Staphylococcus aureus* and *Escherichia coli* through continuous release of GL13K, demonstrating its potential application value in the field of antibacterial therapy [65]. On the other hand, Zhou et al. utilized silanization technology to immobilize the antibacterial peptide GL13K (570 μg/mL) onto titanium surfaces, aiming to enhance the osteogenic integration properties of the material. Experimental results indicated that the GL13K-coated titanium not only promoted the proliferation and migration of BMSCs and HUVECs but also facilitated osteoblast differentiation and angiogenesis leveraging its immunomodulatory potential [43]. To achieve the application effects of GL13K on SIS/HA scaffolds, we immersed the scaffolds in GL13K-FITC solutions of different concentrations (100 μg/mL, 500 μg/mL, 1000 μg/mL, and 1500 μg/mL). Fluorescence microscope observations revealed that the 1000 μg/mL and 1500 μg/mL concentration groups exhibited similar fluorescence intensity and density, indicating that within this concentration range, GL13K can uniformly and maximally bind to the SIS/HA scaffolds. In conclusion, it can be deduced that SIS/HA scaffolds loaded with GL13K (1000 μg/mL) exhibit great potential in terms of superior antimicrobial properties, promotion of cell

migration, and osteogenic and angiogenic effects. Furthermore, the release characteristics of scaffolds loaded with different concentrations of GL13K were analyzed through the release profile of GL13K (Fig. 2I). The standard curve is shown in Figure S2C. The G-SIS/HA + gel-Exos scaffold with a GL13K concentration of 500 μg/mL, although possessing the potential for multifunctional effects such as antibacterial and osteogenic activities, exhibited a relatively short release period for GL13K, achieving complete release within approximately 15 days. In contrast, the G-SIS/HA + gel-Exos scaffold with a concentration of 1000 μg/mL rapidly released about 40.87 ± 4.37 % within the first three days. This rapid release phase ensured that GL13K loaded on the scaffold could be released into the surrounding environment in large amounts in a short time, effectively exerting the local antimicrobial function, and providing favorable establishment for the construction of an osteogenic environment. Subsequently, the release rate of GL13K from the scaffold gradually slowed down, with a sustained release period extending up to 25 days, indicating that GL13K could be stably released over an extended period and continued to exert its effects. The degradation rates of the different scaffolds were evaluated by immersing them in SBF for 6 weeks. The results revealed that the SIS gel exhibited the fastest degradation rate, whereas the Bio-Oss® Collagen, SIS/HA scaffold, SIS/HA + gel scaffold, and G-SIS/HA + gel-Exos scaffold degraded more slowly, with some undegraded material still present until the end of the sixth week (Fig. 2J). This gradual degradation process could provide ample time and space for new bone formation, thereby effectively maintaining the volume of the alveolar ridge. Based on the results of the scaffold characterization, the SIS/HA + gel coaxial scaffold was selected for further *in vitro* and *in vivo* experiments, owing to its superior mechanical properties.

3.3. Biocompatibility and cell behaviors of coaxial composite scaffolds

To elucidate the impact of scaffold materials on cytotoxicity, proliferation, and migratory tendencies, the biocompatibility of various scaffolds (SIS/HA + gel, G-SIS/HA + gel, SIS/HA + gel-Exos, and G-SIS/HA + gel-Exos, with the blank group and Bio-Oss® Collagen as the control) was thoroughly investigated. Fig. 3A presented the schematic representation of cell behaviors on the G-SIS/HA + gel-Exos scaffold. The proliferative activity of both BMSCs and HUVECs was evaluated by the CCK-8 assay. As depicted in Fig. 3B–a notable increase in cell numbers was observed over the extended culture period, particularly in the G-SIS/HA + gel-Exos group, indicating a significant enhancement in cell proliferation. This augmentation is potentially attributed to the pivotal roles played by GL13K and Exos within the scaffold architecture. Notably, the cell proliferation capacity of the SIS/HA + gel group was higher than that of the blank group, which highlights the superiority of SIS as a constituent of the coaxial scaffolds. SIS is enriched with natural collagen and rich in bioactive factors, which endows coaxial scaffolds with the potential ability to promote cell proliferation and excellent biocompatibility [66]. Furthermore, the cytotoxicity of these scaffolds was assessed using live/dead staining experiments. After 1 and 3 days of culture, respectively, BMSCs and HUVECs exhibited growth well in all groups, with a minimal presence of dead cells (Fig. 3C and Figure S3A). The results collectively demonstrated that all scaffold groups exhibited satisfactory biosafety, which was essential for cell survival and subsequent tissue repair *in vivo*.

To investigate the chemotactic response of the coaxial scaffolds to BMSCs and HUVECs, Transwell assay and scratch assay were performed. The results of the Transwell assay showed that, after 24 h of culture, the number of migrating cells in G-SIS/HA + gel, SIS/HA + gel-Exos, and G-SIS/HA + gel-Exos scaffolds was significantly higher than that in the blank group, SIS/HA + gel group, and Bio-Oss® Collagen. Notably, the G-SIS/HA + gel-Exos group exhibited the highest number of migrating cells (Fig. 3D). Quantitative analysis of the migrating cell counts revealed significant differences between the G-SIS/HA + gel, SIS/HA + gel-Exos, and G-SIS/HA + gel-Exos scaffolds, and the blank group, SIS/
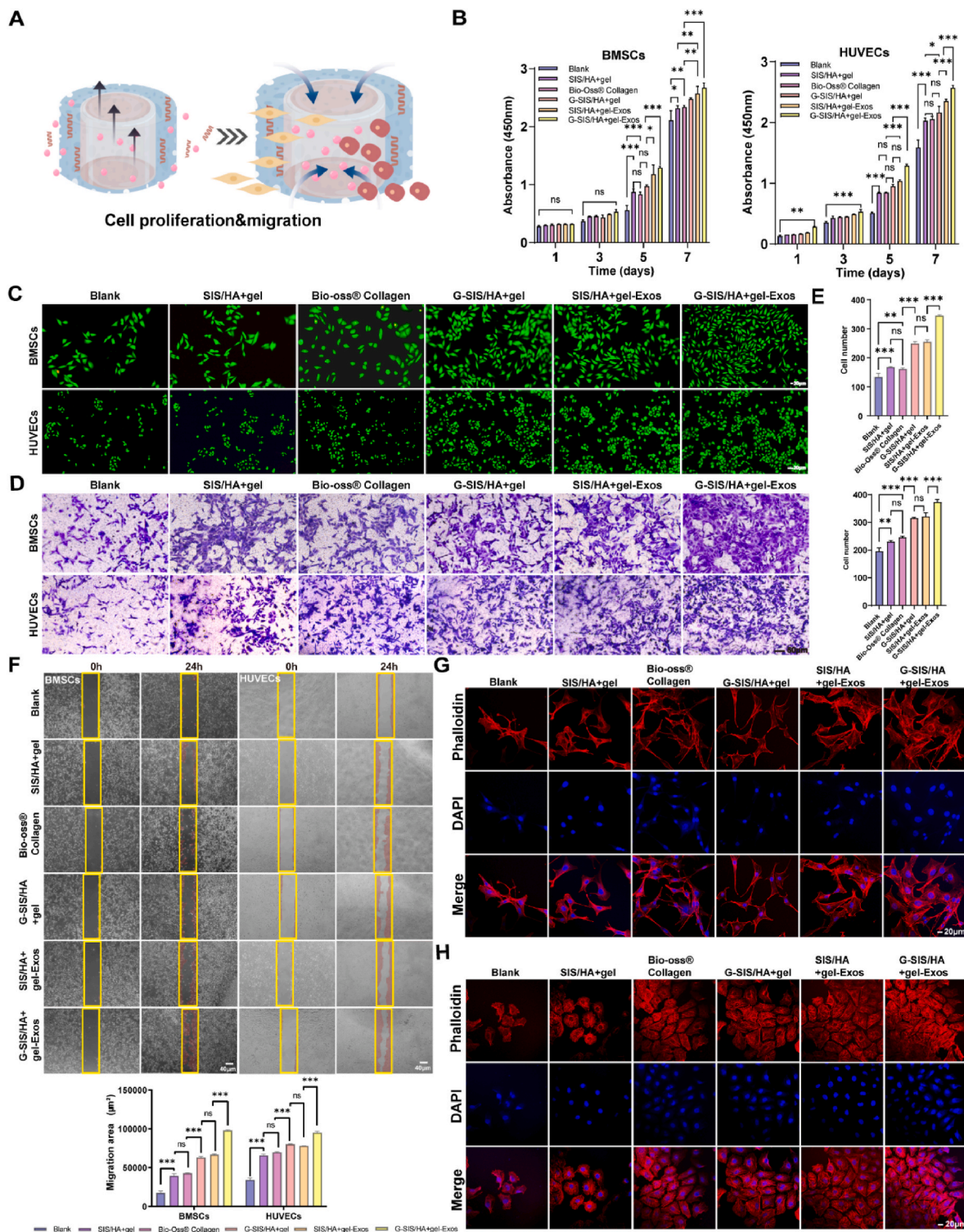
Fig. 3. Proliferation, migration, and morphology of cells on different scaffolds. (A) Schematic representation of cell behavior on G-SIS/HA + gel-Exos scaffolds (B) Cell viability of BMSCs and HUVECs at 1, 3, 5, and 7 days (C) Live and dead staining images of BMSCs and HUVECs cultured with different scaffold extracts (1 day). (D) Migration staining of BMSCs and HUVECs with different scaffold extracts. (E) Quantification of the number of migrated BMSCs and HUVECs. One-way analysis of variance was used for statistical analysis. Data are shown as mean ± SD, *P < 0.05, **P < 0.01, ***P < 0.001*. (F) Scratched wound assay of BMSCs and HUVECs. Quantitative analysis of the area of migration BMSCs and HUVECs. One-way analysis of variance was used for statistical analysis. Data are shown as mean ± SD, *P < 0.05, **P < 0.01, ***P < 0.001*. Cytoskeletal morphology of (G) BMSCs and (H) HUVECs after 3 days of culture. Nuclei (blue), actin filaments (red).

HA + gel group, and Bio-Oss® Collagen, suggesting that GL13K and Exos played a crucial role in promoting cell migration (Fig. 3E) (*P < 0.05*). To further examine the migration capabilities of the cells, a scratch assay was conducted. After 24 h of culture, the migration area of both BMSCs and HUVECs in the G-SIS/HA + gel-Exos group was notably increased compared to the blank control group, SIS/HA + gel group, and Bio-Oss® Collagen (*P < 0.05*) (Fig. 3F). GL13K, an AMP derived from a salivary protein, has been proven to exhibit excellent cellular compatibility

without cytotoxicity, with the ability to recruit cells [67]. Research has indicated that exosomes may participate in cellular proliferation, migration, and matrix synthesis (including chondrocyte synthesis) via the AKT and ERK signaling pathways [68]. The cell morphology and spreading of BMSCs and HUVECs were evaluated by cytoskeleton staining after 3 days of culture on different scaffolds. CLSM images revealed that the number of BMSCs and HUVECs in the G-SIS/HA + gel-Exos group was significantly greater than in the other groups. In comparison to the blank group, the BMSCs in the SIS/HA + gel group, Bio-Oss® Collagen, G-SIS/HA + gel, SIS/HA + gel-Exos, and G-SIS/HA + gel-Exos scaffolds exhibited a fusiform tensile morphology, excellent extensibility, and extended pseudopodia of cells. A dense network of actin filaments was also observable (Fig. 3G). For HUVECs, a smaller expansion area of the cells was observed in the blank group and the cell morphology was not readily apparent. However, in the SIS/HA + gel group, Bio-Oss® Collagen, G-SIS/HA + gel, SIS/HA + gel-Exos, and G-SIS/HA + gel-Exos scaffolds, the HUVECs displayed a polygonal morphology with distinct cell expansion and orderly arranged red actin filaments visible within the cells (Fig. 3H). Consequently, the G-SIS/HA + gel-Exos coaxial scaffold significantly promoted the development of the cytoskeleton of BMSCs and HUVECs, providing an optimal growth environment for these cells.

3.4. Evaluation of tube formation assays

The pro-angiogenic potential of the G-SIS/HA + gel-Exos scaffold was confirmed via the tube formation experiment (Fig. 4A–S4A). After 6 h of culture, HUVECs formed virtually no vessel-like structures in the control group and Bio-Oss® Collagen, whereas a minor quantity of tubules was observed in the SIS/HA + gel group, which might be related to the diverse array of active factors present in SIS, including vascular endothelial growth factor and fibroblast growth factor [69,70]. In the G-SIS/HA + gel, SIS/HA + gel-Exos, and G-SIS/HA + gel-Exos scaffolds, a substantial quantity of vascular-like structures was observed, particularly in the G-SIS/HA + gel-Exos group, where a greater number of tubules with a more complete tubular structure were formed. Furthermore, the pro-angiogenic capacity of the G-SIS/HA + gel-Exos scaffold was further evaluated at the protein level. Western blot results (Fig. 4B and C) showed that the expression of angiogenesis-related proteins (HIF-1α and VEGF) was gradually up-regulated in G-SIS/HA + gel, SIS/HA + gel-Exos, and G-SIS/HA + gel-Exos scaffolds. Notably, the expression levels in the G-SIS/HA + gel-Exos group were significantly higher compared to the control group and the SIS/HA + gel group ($P < 0.05$). Additionally, immunofluorescence analysis (Fig. 4D–F) demonstrated that the fluorescence intensities of HIF-1α and VEGF in the G-SIS/HA + gel-Exos group were substantially greater than those in the other groups, and the fluorescence intensities of G-SIS/HA + gel and SIS/HA + gel-Exos scaffolds were close. From the gene level, the expression levels of angiogenesis-related genes were assessed by PCR assay. The results in Fig. 4G showed that the mRNA expression levels (HIF-1α and VEGF) in the G-SIS/HA + gel-Exos group were significantly higher than those in the other groups ($P < 0.05$). The above results suggested that the concurrent administration of GL13K and Exos plays an important role in promoting angiogenesis.

In the process of osteogenesis, angiogenesis and bone regeneration are closely coupled. The emergence of new blood vessels is pivotal in providing oxygen, nutrients, and growth factors necessary for bone regeneration, thus fostering the development of vascularized bone structures and ensuring efficient healing and functional restoration of bone defects [71]. VEGF, as one of the most important growth factors in angiogenesis, induces endothelial cell proliferation and migration while indirectly stimulating new bone formation. Additionally, HIF-1α induced by a hypoxic environment can enhance osteogenesis by regulating the expression of VEGF [72,73]. According to Pan et al., miR-NA29a in BMSCs-Exos could reduce HDAC4de expression, and significantly up-regulate RUNX2 and VEGF, playing a role in

angiogenesis [74]. Furthermore, Zhou et al. found that constructing a GL13K coating on the titanium surface enhanced the expression of genes such as VEGF-A and HIF-1α, promoting of angiogenesis [47]. Therefore, hydrogel rich in BMSCs-Exos on the inner layer of the scaffold combined with SIS/HA on the outer layer loaded with GL13K has the potential to up-regulate the expression of genes related to angiogenesis, effectively promoting scaffold vascular network formation and accelerating bone remodeling.

3.5. In vitro osteogenic differentiation of BMSCs by coaxial composite scaffolds

The osteogenic potential of different scaffolds was evaluated through the utilization of ALP staining, ARS staining, Western blot, and qRT-PCR. ALP is a crucial marker for osteoblast differentiation and maturation during osteogenic differentiation [75]. Microscopic pictures of ALP staining were shown in Fig. 5A. On days 7 and 14, the G-SIS/HA + gel-Exos group displayed the most profound staining, followed by Bio-Oss® Collagen, G-SIS/HA + gel, and SIS/HA + gel-Exos scaffolds, whereas the SIS/HA + gel group exhibited a slightly darker tint compared to the blank group, which could be ascribed to the presence of HA in the SIS/HA scaffold. Studies have shown that HA-incorporating composite materials, due to their biomimetic characteristics, are capable of activating nucleation sites, increasing the apatite nucleation rate, and enhancing the expression of ossification-related markers, thereby ultimately fostering bone formation [76,77]. A comparable trend to ALP staining was observed in the ARS results (Fig. 5B). On day 14, all groups exhibited scattered calcium nodule deposits, among which the G-SIS/HA + gel-Exos group displayed the highest number of calcium nodules. By day 21, a marked increase in calcium nodules was noted in all groups compared to day 14, with large calcium nodules predominantly found in the G-SIS/HA + gel-Exos group. This augmentation could be attributed to the stimulatory influence of GL13K and Exos on osteogenic differentiation and mineral deposition of BMSCs.

To further elucidate the impact of different scaffolds on the expression of osteogenesis-related proteins, Western blot analysis revealed (Fig. 5C and D) that the G-SIS/HA + gel-Exos group exhibited the highest expression levels of osteogenesis-related proteins (BMP2, ALP, OPN, and RUNX2) ($P < 0.05$). In contrast, the protein expression levels in the G-SIS/HA + gel group and the SIS/HA + gel-Exos group were nearly identical, with no significant differences ($P > 0.05$). The results of qRT-PCR also confirmed this trend (Fig. 5E), demonstrating a significant upregulation in the expression levels of osteogenesis-related mRNAs (BMP2, ALP, OPN, and RUNX2) in the G-SIS/HA + gel-Exos group, surpassing those in the other four groups ($P < 0.05$). The primer sequence used in the experiment was provided in Table S1. Furthermore, immunofluorescence staining images validated the expression of osteogenesis-related proteins (BMP2, ALP, and RUNX2). Specifically, the strongest red fluorescence was observed in the BMSCs of the G-SIS/HA + gel-Exos group ($P < 0.05$), indicating a high level of protein expression (Fig. 5F–S4B).

Proteomics and genomic analyses have confirmed that microRNAs (miRNAs) and proteins within BMSCs-Exos constitute crucial elements that facilitate bone repair processes [78]. In-depth investigations by Lu et al. revealed that BMSCs-Exos carrying miR29a exhibit remarkable potential in regulating angiogenesis and osteogenesis, and may serve as a potential therapeutic target for osteoporosis [79]. Additionally, research conducted by Ma et al. demonstrated the successful reconstruction of cranial bone defects in rats through the specific binding of BMSCs-Exos to SIS membranes modified with engineered recombinant peptides. The underlying mechanism suggests that exosomes in this process may mediate osteogenic effects via the PI3K/Akt/mTOR signaling pathway [80]. In addition, experimental results in a rat model of periodontitis showed that BMSCs-Exos also exhibit notable bone repair efficacy, enhancing the migration, proliferation, and osteogenic differentiation of human periodontal ligament stem cells (hPDLCs). This
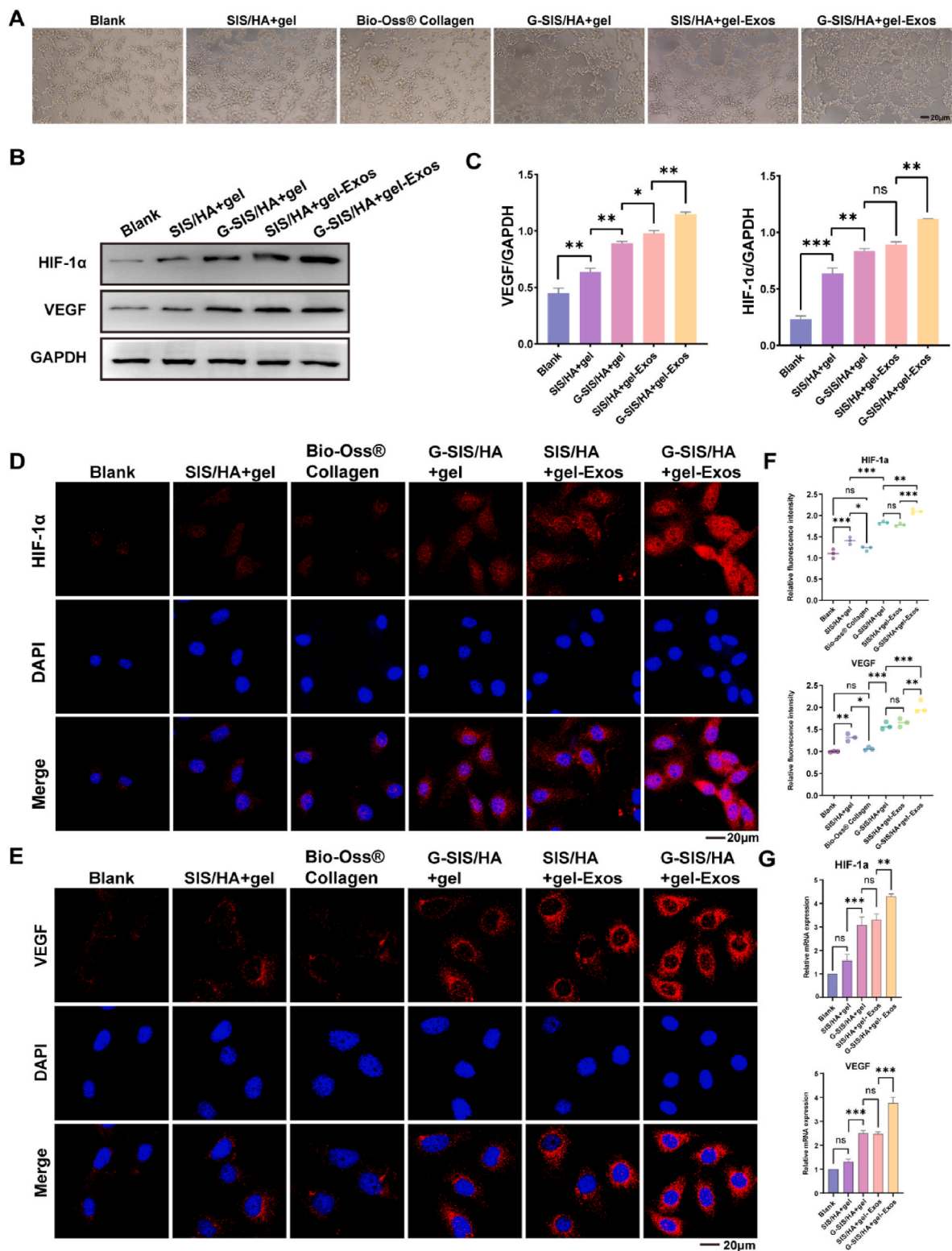
Fig. 4. Promotion of angiogenesis *in vitro*. (A) HUVECs were cultured on Matrigel for 6 h to form microtubules. (B) Expression of angiogenic related proteins (HIF-1α and VEGF) by Western blot analysis. (C) Quantitative analysis of Western blot experiments. Data are shown as mean ± SD, *P <0.05, **P <0.01, ***P <0.001. Expression of angiogenesis-related proteins HIF-1α (D) and VEGF (E) was observed by immunofluorescence. (F) Quantitative analysis of fluorescence intensity. Data are shown as mean ± SD, *P <0.05, **P <0.01, ***P <0.001. (G) Expression of genes related to angiogenesis (HIF-1α and VEGF). Data are shown as mean ± SD, *P <0.05, **P <0.01, ***P <0.001.
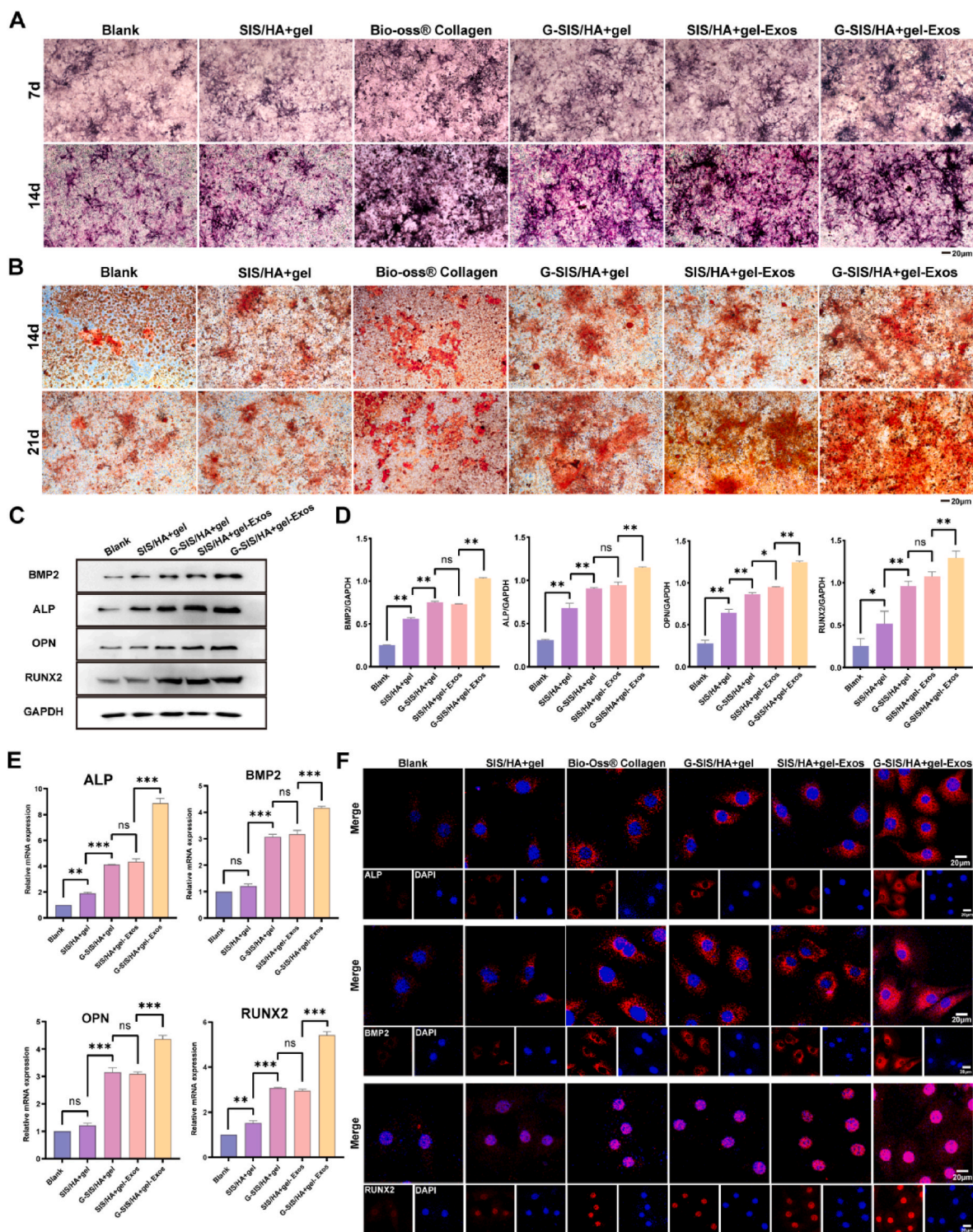
Fig. 5. Studies on osteogenic differentiation *in vitro*. (A) ALP staining images of different scaffolds at 7 and 14 days. (B) ARS staining images of different scaffolds on 14 and 21 days. (C) Western blot analysis for expression of osteogenesis-related proteins (BMP2, ALP, OPN, and RUNX2) (D) Quantitative analysis of Western blot analysis. Data are shown as mean ± SD, *$P < 0.05$, **$P < 0.01$, ***$P < 0.001$. (E) qRT-PCR detection of expression levels of osteogenic-related genes (BMP2, ALP, OPN, and RUNX2). Data are shown as mean ± SD, *$P < 0.05$, **$P < 0.01$, ***$P < 0.001$. (F) Immunofluorescence assays of proteins related to osteogenesis.

may occur through the modulation of the OPG-RANKL-RANK signaling pathway, thereby promoting periodontal tissue regeneration [81]. On the other hand, GL13K, an antibacterial peptide, has previously been shown to possess osteogenic capabilities, stimulating the proliferation and migration of BMSCs, upregulating the expression of osteogenic-related genes and proteins (ALP, OPN, and OCN), and

enhancing osteogenic differentiation [65]. This study further underscores the supportive role of coaxial scaffold systems in promoting the proliferation and osteogenic differentiation of bone marrow mesenchymal stem cells. Notably, when compared to SIS/HA scaffolds, the G-SIS/HA + gel-Exos scaffold, incorporating both GL13K and Exos, significantly enhances the osteogenic differentiation capabilities of cells

through the synergistic effects of these dual factors.

3.6. In vitro antimicrobial activity of coaxial composite scaffolds

The oral cavity serves as a home to a multitude of microorganisms, necessitating the prevention of infections associated with the implantation of scaffolds [82]. During the implantation process, multiple bacterial species have the potential to adhere to the biological material, ultimately leading to infection. Among these, *S. aureus*, a gram-positive aerobic bacterium, stands out as a prevalent pathogenic bacterium

associated with implanted biomaterial infections [83,84]. Furthermore, *F. nucleatum* and *S. sanguis* are frequently encountered as gram-negative anaerobes and gram-positive facultative anaerobes, respectively, in the oral cavity [82]. To investigate the antibacterial activity of coaxial scaffolds, we employed the aforementioned bacteria as representatives and evaluated them by performing SEM, plate colony counting, bacterial live/dead staining, and zone of inhibition experiments.

To visually demonstrate the antibacterial properties of the scaffolds, SEM was employed to observe the distribution and morphology of *S. aureus*, *S. sanguis*, and *F. nucleatum* on different scaffold surfaces. As
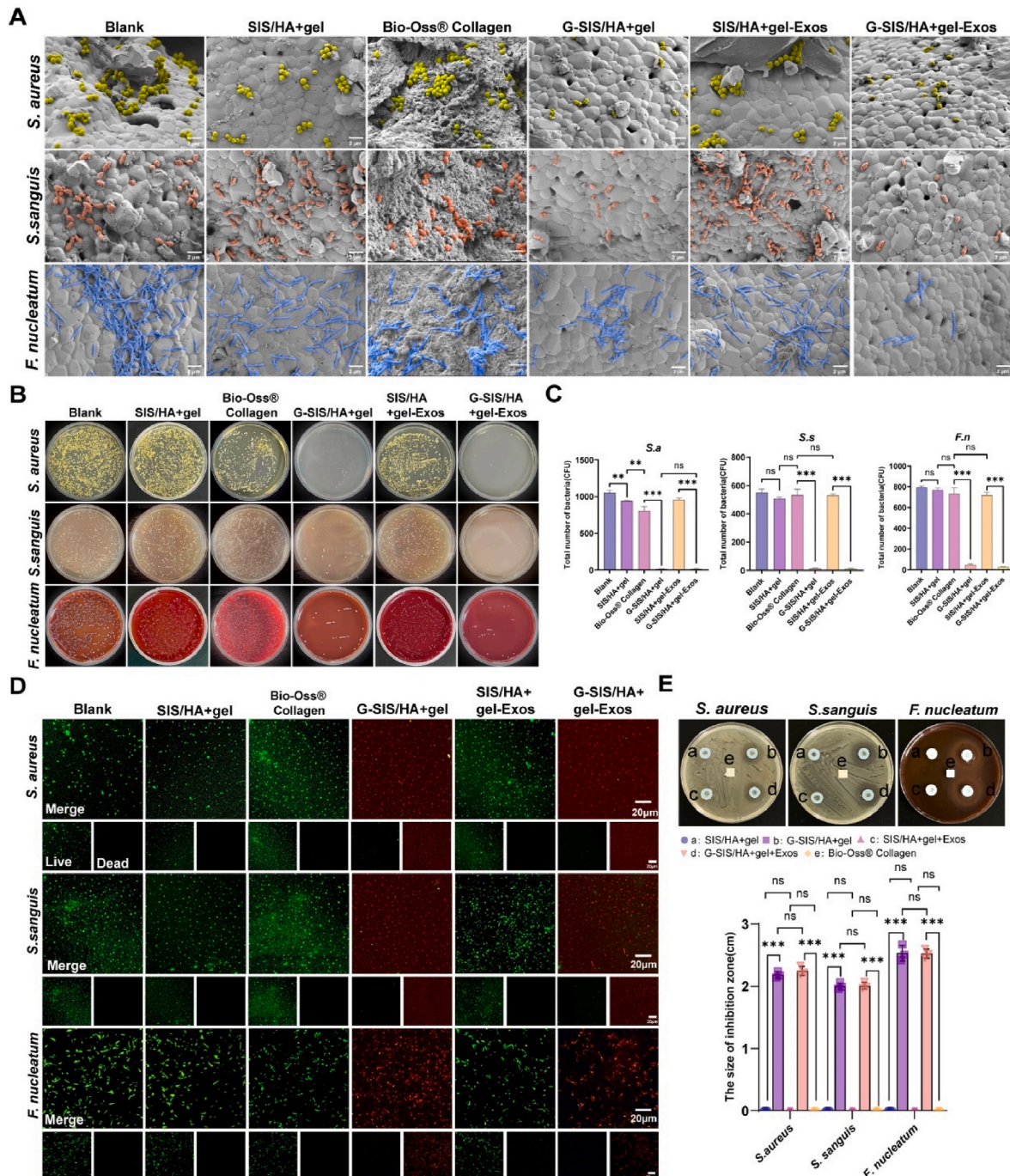

Fig. 6. *In vitro* antibacterial activity (A) SEM image. (B) Plate counts of bacterial colonies (*S. aureus*, *S. sanguis*, and *F. nucleatum*). (C) Quantitative analysis of bacterial colonies. Data are shown as mean ± SD, *$P < 0.05$, **$P < 0.01$, ***$P < 0.001$. (D) CLSM images of *S. aureus*, *S. sanguis*, and *F. nucleatum* live/dead staining. Green: live bacteria, red: dead bacteria. (E) Inhibition zones of *S. aureus*, *S. sanguis*, and *F. nucleatum* co-cultured with different scaffolds and statistical analysis of the inhibition zones. (a: SIS/HA + gel, b: G-SIS/HA + gel, c: SIS/HA + gel-Exos, d: G-SIS/HA + gel-Exos, e: Bio-Oss® collagen) Data are shown as mean ± SD, *$P < 0.05$, **$P < 0.01$, ***$P < 0.001$.

shown in Fig. 6A, the surfaces of the blank group, SIS/HA + gel group, Bio-Oss® Collagen, and SIS/HA + gel-Exos group exhibited abundant bacterial adhesion with intact bacterial membranes, while the bacterial count on the surfaces of the G-SIS/HA + gel group and G-SIS/HA + gel-Exos group significantly decreased, displaying bacterial rupture,

deformation, or wrinkled bacterial surfaces. Plate colony counting results (Fig. 6B and C) revealed that compared with the blank group, SIS/HA + gel group, Bio-Oss® Collagen, and SIS/HA + gel-Exos group, the number of bacterial colonies in the G-SIS/HA + gel group and G-SIS/HA + gel-Exos group was significantly reduced, with only a small number of
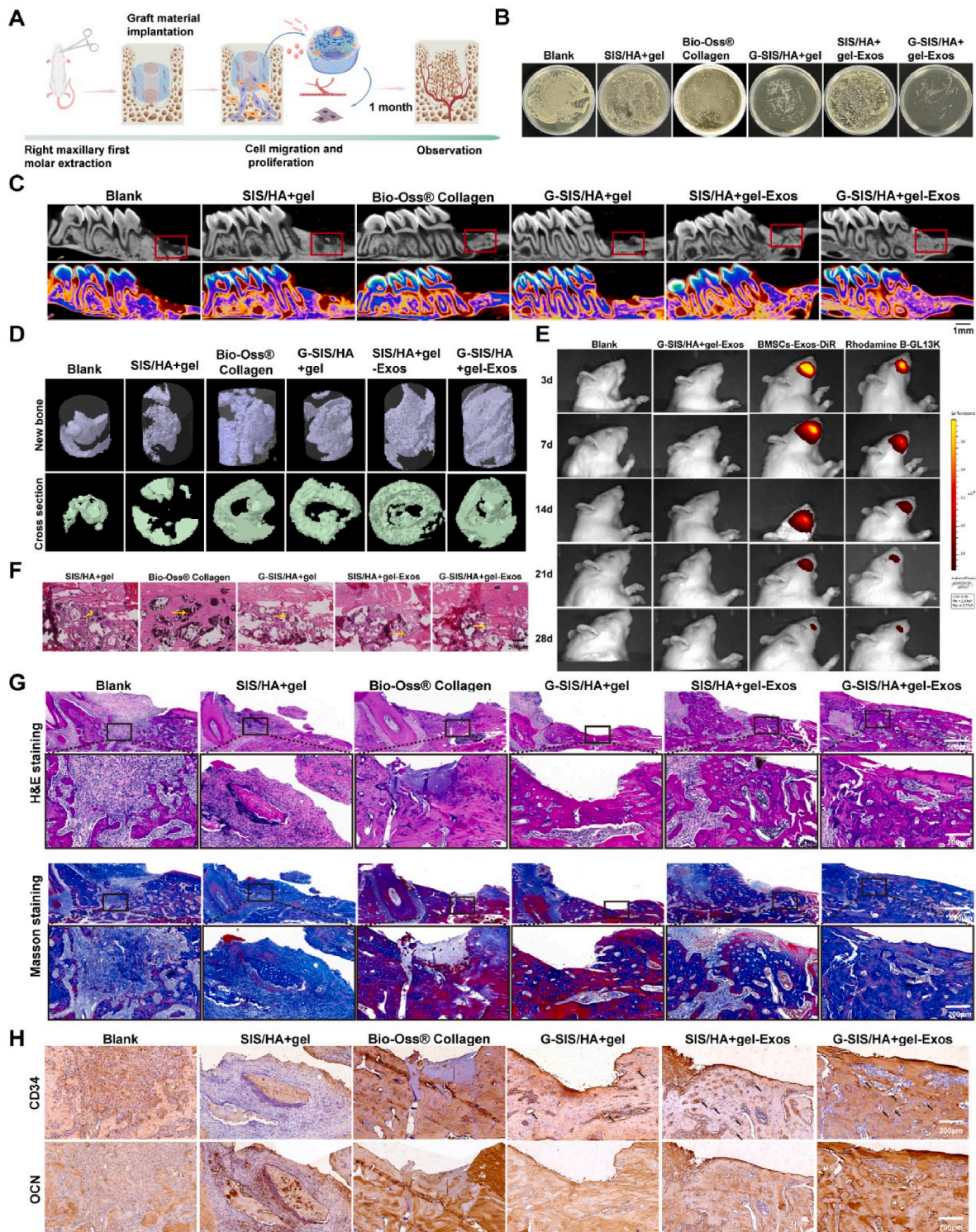

Fig. 7. Evaluation and analysis of post-extraction and alveolar reconstruction. (A) Schematic diagram of the experiment. (B) Colony counts at the wound sites. (C) Sagittal picture of the rat maxilla. (D) Three-dimensional reconstructed images of rat alveolar bone defects. (E) G-SIS/HA + gel-Exos materials (Rhodamine B-GL13K, DiR-Exos) were implanted into a rat extraction socket and the release of GL13K and Exos was observed *in vivo* at different time points. (F) Subcutaneous degradation of different scaffolds in rats (Yellow arrows represent undegraded materials). (G) The newly formed bone tissue was evaluated by H&E staining and Masson's trichrome staining after an operation of 1 month. (H) Immunohistochemical analysis of CD34 and OCN expression.

bacterial colonies visible ($P < 0.05$). Further evaluation of the antibacterial effect of coaxial scaffolds loaded with GL13K was conducted by live/dead bacterial staining. Fig. 6D showed that the blank group, SIS/HA + gel group, Bio-Oss® Collagen, and SIS/HA + gel-Exos group had significantly more live bacteria, while the G-SIS/HA + gel group and G-SIS/HA + gel-Exos group had a higher proportion of dead bacteria. The zone of inhibition experiment results (Fig. 6E) showed that no inhibition zones were observed around the scaffolds in the blank group, SIS/HA + gel group, Bio-Oss® Collagen, and SIS/HA + gel-Exos group, while clear inhibition zones were observed around the scaffolds in the G-SIS/HA + gel group and G-SIS/HA + gel-Exos group when placed in three different bacterial plates. Statistical analysis showed no significant difference in the diameter of the inhibition zones between the G-SIS/HA + gel group and the G-SIS/HA + gel-Exos group, but significant differences were observed compared to the other three groups ($P < 0.05$).

Most AMPs perforate the bacterial membrane by targeting its negatively charged portion, disrupting its integrity and leading to bacterial lysis and death [85]. The results of the above experiments indicate that the scaffold containing GL13K has a significant antibacterial effect on the associated bacteria during implantation. In the initial stage of scaffold implantation, the G-SIS/HA + gel-Exos coaxial scaffold can rapidly and greatly release GL13K from the scaffold, so that GL13K around the scaffold reaches a local high concentration level in the initial stage and is slowly released in the later stage, which effectively kills the gram-positive and gram-negative bacteria adhered to and around the scaffold surface, which provides a favorable platform for the later bone repair process. In a previous study, Qi et al. achieved excellent antibacterial effects against localized Staphylococcus aureus and Escherichia coli at infected wounds using HAMA (hyaluronate methacrylate) hydrogel to deliver tFNA (tetrahedral framework nucleic acid)-loaded antimicrobial peptide GL13K [86]. Therefore, compared with the application of antibiotics, GL13K as a cationic antimicrobial peptide avoids the risk of bacterial resistance and plays an antibacterial role more safely and effectively.

3.7. In vivo alveolar bone regeneration assessment

A rat tooth extraction model was used to assess the bone-inducing potential of the scaffolds *in vivo* (Figure S5A). A schematic illustration of the experimental design is shown in Fig. 7A. Three days after implantation of the material, colony counts at the wound sites were performed to assess the antimicrobial effects of the different scaffolds. As illustrated in Fig. 7B–a large number of colonies were visible in control and unloaded GL13K groups compared with G-SIS/HA + gel and G-SIS/HA + gel-Exos, indicating that the G-SIS/HA + gel-Exos scaffolds exerted an effective antimicrobial effect after implantation in the alveolar socket, providing favorable conditions for subsequent bone reconstruction ($P < 0.05$) (Figure S5C). After a month, the observation of rat tooth extraction wounds demonstrated that they had grown well, tooth extraction sockets in periodontal healing, and were tough (Figure S5B). Analysis of the sagittal views of the extraction sockets using Dataview revealed varying degrees of new bone formation in the experimental groups with scaffold implantation (Fig. 7C). Conversely, the blank group exhibited significant horizontal resorption of the alveolar bone, with only a minimal amount of regenerated bone visible at the base of the extraction socket, resulting in a concave appearance. Notably, the Bio-Oss® collagen group showed alveolar bone neogenesis, similar to the osteogenic effect of the G-SIS/HA + gel-Exos scaffold. This result further confirmed the superiority of Bio-Oss® Collagen for alveolar ridge preservation.

To illustrate the regenerative effect of the coaxial scaffold in the bone defect, a 3D model of the newly formed bone tissue was constructed (Fig. 7D). The bone repair amount in the alveolar socket of the blank group was less than that of the other groups, and the G-SIS/HA + gel-Exos group exhibited the most significant bone regeneration effect. In horizontal sections, as the reconstruction process progressed, the new

bone growth in the SIS/HA, G-SIS/HA + gel, SIS/HA + gel-Exos scaffolds, and Bio-Oss® Collagen groups showed a tendency to gradually advance towards the central region of the defect, with less osteogenesis observed at the defect's center, whereas the G-SIS/HA + gel-Exos group exhibited a denser distribution of new bone tissue in the central region of the defect. This finding was consistent with our previous hypothesis that BMSCs-Exos in the SIS gel within the coaxial scaffolds promoted the proliferation and migration of cells to the scaffolds and played an important role in the osteogenesis process. According to the quantitative analysis of Micro-CT, the bone volume/total volume (BV/TV), bone mineral density (BMD), and trabecular thickness (Tb. Th) of different groups were compared. The results showed that in terms of BV/TV, implanted scaffold groups were all higher than the blank group, and G-SIS/HA + gel-Exos group was the highest among all groups. The Bio-Oss® Collagen group had slightly higher BMD than the G-SIS/HA + gel-Exos group. The trabecular thickness of the Bio-Oss® Collagen, G-SIS/HA + gel, SIS/HA + gel-Exos, and G-SIS/HA + gel-Exos groups was higher than that in the SIS/HA + gel and blank groups, and there was statistical difference ($P < 0.05$) (Figure S5D). Utilizing fluorescence imaging technology, we evaluated the *in vivo* release characteristics of GL13K and BMSCs-Exos within the alveolar sockets of rats (Fig. 7E). The results demonstrated that on the third day post-implantation, strong fluorescence signals were detected for both GL13K and BMSCs-Exos within the coaxial scaffolds. Over time, these fluorescence signals gradually diminished, revealing the dynamic process of drug release. The fluorescence signal remained significant until day 14, implying that GL13K and BMSCs-Exos in the scaffolds had not been fully released. When the time reached the twenty-eighth day, the fluorescent signals had become very weak, indicating that GL13K and BMSCs-Exos in the scaffolds implanted into the tooth extraction sockets were nearly completely released. Notably, at the same time points, the fluorescence intensity of GL13K was weaker than that of BMSCs-Exos, indicating a slower release of BMSCs-Exos from the hydrogel within the hollow portion of the scaffold. This slow release ensured the long-term stability of the therapeutic effect of BMSCs-Exos. To evaluate the degradation characteristics and biocompatibility of different scaffold materials *in vivo*, coaxial scaffolds were implanted into the subcutaneous tissue of rats, with Bio-Oss® Collagen serving as the control. Four weeks later, the samples were harvested and stained for observation. As shown in Fig. 7F, residual material was visible in the Bio-Oss® Collagen group, with extensive ingrowth of fibrous connective tissue and a small amount of inflammatory cell infiltration within the material. In the coaxial scaffold group, the scaffold material was also not fully degraded, and hydroxyapatite particles were still observable at the implantation site, accompanied by the ingrowth of fibrous connective tissue. This is consistent with data from *in vitro* degradation experiments. Notably, none of the groups showed significant inflammatory responses, indicating their good biocompatibility and ability to exist relatively stably in the *in vivo* environment without eliciting excessive immune responses. Additionally, four weeks after subcutaneous implantation, histological staining analysis of major organs (including the heart, liver, and kidneys) was conducted to assess the biocompatibility of the coaxial scaffold materials. As shown in Figure S6A, the major organs in all experimental groups exhibited normal morphological structures histologically, with no abnormal changes or intergroup differences observed, suggesting the good biosecurity of the coaxial scaffolds.

The analysis of new bone formation was conducted through H&E and Masson's trichrome staining (Fig. 7G). After a month, it was observed that the blank and SIS/HA + gel groups exhibited limited bone tissue formation within the defect, predominantly filled with fibrous connective tissue. Conversely, the G-SIS/HA + gel-Exos group displayed superior new bone formation and mineralization, accompanied by the presence of blood vessels. Immunohistochemical staining was employed to evaluate the expression of osteogenic and angiogenic genes, with OCN and CD34 being specific osteogenic markers and markers of endothelial progenitor cell formation during neoangiogenesis, respectively [87,88].

As depicted in Fig. 7H, the G-SIS/HA + gel and SIS/HA + gel-Exos groups exhibited a significantly higher expression of OCN and CD34 compared to the blank and SIS/HA + gel groups, with the G-SIS/HA + gel-Exos group displaying the most prominent expression. This finding indicated the effectiveness of G-SIS/HA + gel-Exos scaffolds in promoting osteogenesis and angiogenesis in the extraction socket site. The results underscored the superior osteogenic and bone integration

capabilities of the coaxial scaffold. Moreover, the synergistic effect of GL13K and BMSCs-Exos significantly accelerated bone tissue remodeling, resulting in a marked increase in new bone tissue.

3.8. Gene expression and bioinformatic analyses

Based on both *in vitro* and *in vivo* experimental results, the G-SIS/HA
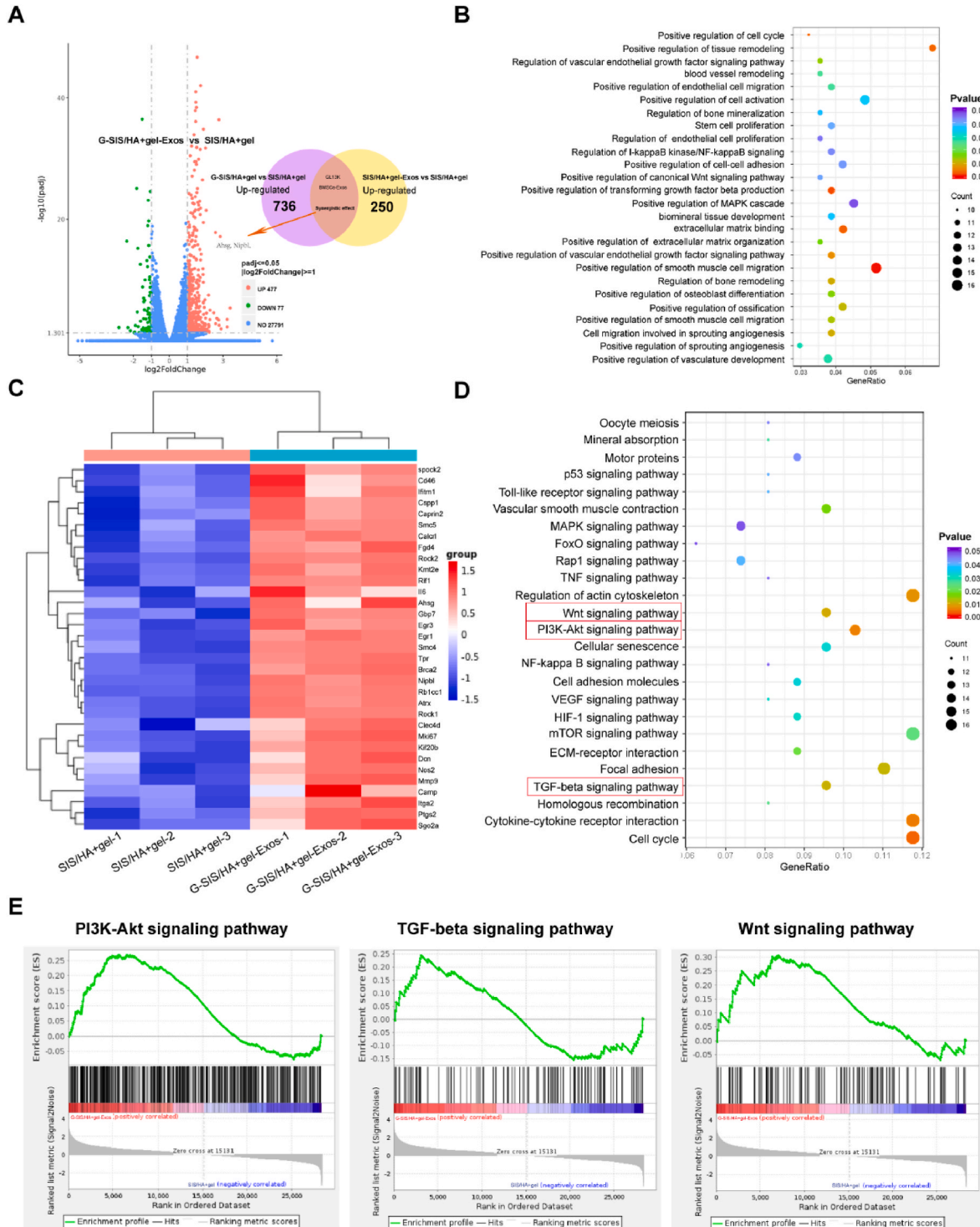

Fig. 8. Gene expression and analysis of biological activity of BMSCs cultured in SIS/HA + gel and G-SIS/HA + gel-Exos groups. (A) Venn diagrams and volcano plots of genes affected by coaxial scaffolding. (B) Representative enriched GO up terms of DEGs from SIS/HA + gel versus G-SIS/HA + gel-Exos. (C) Heatmap of DEGs related to cellular activity, angiogenesis and osteogenesis from SIS/HA + gel versus G-SIS/HA + gel-Exos. (D) The enriched KEGG pathways of DEGs from SIS/HA + gel versus G-SIS/HA + gel-Exos. (E) GSEA plots of SIS/HA + gel versus G-SIS/HA + gel-Exos.

+ gel-Exos scaffold exhibited optimal angiogenic and osteogenic capabilities, attributed to the combined effects of GL13K and BMSCs-Exos. Consequently, we further explored the potential regulatory mechanisms of the coaxial scaffold through RNA sequencing. The volcano plot revealed that, compared to the SIS/HA + gel group, 477 genes were significantly upregulated and 77 genes were downregulated in the G-SIS/HA + gel-Exos experimental group, suggesting significant differences between the two groups (Fig. 8A). To further evaluate the synergistic effects of GL13K and BMSCs-Exos, we used a Venn diagram to display the upregulated differentially expressed genes (DEGs). Specifically, the purple circle represented DEGs upregulated by GL13K, and the yellow circle represented DEGs upregulated by BMSCs-Exos. These overlapping genes were located among those up-regulated in the volcano map by the combined effects of GL13K and BMSCs-Exos, including genes associated with osteogenesis (Ahsg, Nipbl, etc.), suggesting significant synergism between GL13K and BMSCs-Exos. According to Gene Ontology (GO) enrichment analysis, we found genes related to cell proliferation and migration (positive regulation of vascular smooth muscle cell proliferation, positive regulation of endothelial cell migration, positive regulation of cell activation, etc.), angiogenesis (positive regulation of vasculature development, positive regulation of sprouting angiogenesis), and osteogenic differentiation (positive regulation of osteoblast differentiation, positive regulation of ossification, regulation of bone mineralization, etc.) to be upregulated in G-SIS/HA + gel-Exos (Fig. 8B). Subsequently, a corresponding heatmap was generated for highly expressed DEGs to display the upregulated genes between the two groups (SIS/HA + gel and G-SIS/HA + gel-Exos), including those related to cell proliferation and migration (Egr1, Mmp9, etc.), extracellular matrix (Spock2, Dcn, etc.), and osteogenesis (Ahsg, Nipbl, etc.) (Fig. 8C). Additionally, we enriched the DEGs between the SIS/HA + gel and G-SIS/HA + gel-Exos groups using the KEGG database. The enriched signaling pathways are shown in Fig. 8D, indicating that the G-SIS/HA + gel-Exos group enriches pathways related to cell proliferation and migration (cell cycle, ECM-receptor interaction, FoxO signaling pathway), angiogenesis (HIF-1α, VEGF signaling pathway), and osteogenic differentiation (PI3K-Akt signaling pathway, TGF-β signaling pathway, Wnt signaling pathway, MAPK signaling pathway) [89–91]. Among them, the PI3K-Akt signaling pathway and the transforming growth factor (TGF-β) pathway were significantly enriched, which are closely related to osteogenesis[92–94]. Zhang et al. found that the PI3K-Akt signaling pathway played a key role in the osteogenic effect of exosome/β-TCP scaffolds on BMSCs [95]. Furthermore, the TGF-β signaling pathway has been reported to have specific roles in osteoblast and chondrocyte differentiation and skeletal development. During signal transduction, TGF-β binds to TNF receptor factors, activating TGFβ-activated kinase 1 (TAK1), which then phosphorylates mitogen-activated protein kinases (MAPK) or phosphoinositide 3-kinases (PI3K), further activating target transcription factors (NF-κB, RUNX2) [96]. Accordingly, gene set enrichment analysis (GSEA) further confirmed that more genes involved in pathways such as the PI3K-Akt pathway and the TGF-β pathway were up-regulated in the up-regulated regions of the G-SIS/HA + gel group compared to the SIS/HA + gel group, and the association was stronger (Fig. 8E). In summary, the RNA-seq results are consistent with the aforementioned *in vitro* and *in vivo* experimental results, suggesting that G-SIS/HA + gel-Exos holds promise for homing endogenous cells, inducing angiogenesis, and bone regeneration.

4. Conclusion

In summary, we have prepared an SIS/HA composite hydrogel coaxial scaffold that achieved dual optimization of structural strength and biological activity through its unique structural design and functional modification. With the effects of GL13K and BMSCs-Exos, it not only effectively exerts antibacterial properties but also promotes the formation of new bone and blood vessels in both the inner and outer regions of the scaffold, thereby shortening the alveolar bone repair time and avoiding insufficient bone formation in the central area of bone defects. The coaxial scaffold demonstrated potential *in vitro* experiments for promoting cell proliferation and migration, angiogenesis, and bone formation. *In vivo* experiments, G-SIS/HA + gel-Exos could effectively rebuild bone defects and achieve bone repair in rat extraction sockets within one month (BV/TV = 80.508 ± 3.04 %). We believe that this comprehensive bone repair platform with excellent mechanical strength and certain deformation capability, integrating multiple functions such as antibacterial activity, angiogenesis, and efficient osteogenic differentiation induction, may provide new insights into the preservation of alveolar socket bone volume following tooth extraction in clinical practice.

CRediT authorship contribution statement

Shiqing Ma: Writing – review & editing, Writing – original draft, Visualization, Validation, Supervision, Software, Resources, Project administration, Methodology, Investigation, Funding acquisition, Formal analysis, Data curation, Conceptualization. **Yumeng Li:** Writing – review & editing, Writing – original draft, Visualization, Validation, Supervision, Software, Resources, Project administration, Methodology, Investigation, Formal analysis, Data curation, Conceptualization. **Shiyu Yao:** Writing – review & editing, Writing – original draft, Visualization, Validation, Supervision, Software, Resources, Project administration, Investigation, Data curation, Conceptualization. **Yucheng Shang:** Writing – review & editing, Visualization, Validation, Supervision, Software, Resources, Methodology, Data curation, Conceptualization. **Rui Li:** Supervision, Software, Resources, Formal analysis, Data curation, Conceptualization. **Lijuan Ling:** Writing – review & editing, Writing – original draft, Visualization, Validation, Supervision, Resources, Conceptualization. **Wei Fu:** Validation, Software, Resources, Project administration, Methodology, Investigation, Funding acquisition. **Pengfei Wei:** Validation, Supervision, Software, Resources. **Bo Zhao:** Writing – review & editing, Writing – original draft, Visualization, Validation, Supervision, Resources, Investigation, Formal analysis, Conceptualization. **Xuesong Zhang:** Visualization, Validation, Software, Project administration, Methodology, Investigation, Formal analysis, Data curation, Conceptualization. **Jiayin Deng:** Visualization, Validation, Supervision, Resources, Project administration, Methodology, Funding acquisition, Formal analysis, Data curation, Conceptualization.

Ethics approval and consent to participate

To evaluate the potential of the coaxial scaffold on the repair of alveolar bone defects in rats. Sprague-Dawley (SD) male rats were selected for animal experiments. All experiments in our work were approved by the Animal Ethics and Welfare Committee of Tianjin Medical University.

Declaration of competing interest

The authors declare the following personal relationships which may be considered as potential competing interests: Pengfei Wei and Bo Zhao are currently employed by Beijing Biosis Healing Biological Technology Co., Ltd.

Acknowledgements

Appendix A. Supplementary data

Supplementary data to this article can be found online at https://doi.org/10.1016/j.bioactmat.2024.12.008.

References

[1] C. Aribau-Gumà, A. Jorba-García, A. Sánchez-Torres, M.À. Sànchez-Garcés, Alveolar ridge preservation: an overview of systematic reviews, Int. J. Oral Maxillofac. Surg. 51 (2022) 234–242, https://doi.org/10.1016/j.ijom.2021.06.002.

[2] R.E. Wang, N.P. Lang, Ridge preservation after tooth extraction, Clin. Oral Implants Res. 23 (2012) 147–156, https://doi.org/10.1111/j.1600-0501.2012.02560.x.

[3] M.G. Araújo, D.R. Dias, F. Matarazzo, Anatomical characteristics of the alveolar process and basal bone that have an effect on socket healing, Periodontology 93 (2023) 277–288, https://doi.org/10.1111/prd.12506, 2000.

[4] V. Chappuis, M.G. Araújo, D. Buser, Clinical relevance of dimensional bone and soft tissue alterations post-extraction in esthetic sites, Periodontology 73 (2017) 73–83, https://doi.org/10.1111/prd.12167, 2000.

[5] J. Gu, K. Jiao, J. Li, J. Yan, K. Wang, F. Wang, Y. Liu, F.R. Tay, J. Chen, L. Niu, Polyphosphate-crosslinked collagen scaffolds for hemostasis and alveolar bone regeneration after tooth extraction, Bioact. Mater. 15 (2022) 68–81, https://doi.org/10.1016/j.bioactmat.2021.12.019.

[6] S. Jana, R. Shah, R. Thomas, A.B.T. Kumar, D.S. Mehta, Techniques for preservation of post-extraction alveolar bone loss: a literature review, JAMMR (2021) 33–42, https://doi.org/10.9734/jammr/2021/v33i1030907.

[7] M.R. Fok, G. Pelekos, L. Jin, Efficacy of alveolar ridge preservation in periodontally compromised molar extraction sites: a systematic review and meta-analysis, J. Clin. Med. 13 (2024) 1198, https://doi.org/10.3390/jcm13051198.

[8] S. Barootchi, L. Tavelli, J. Majzoub, M. Stefanini, H.-L. Wang, G. Avila-Ortiz, Alveolar ridge preservation: complications and cost-effectiveness, Periodontology 92 (2023) 235–262, https://doi.org/10.1111/prd.12469, 2000.

[9] S. Kim, S.-G. Kim, Advancements in alveolar bone grafting and ridge preservation: a narrative review on materials, techniques, and clinical outcomes, Maxillofac Plast Reconstr Surg 46 (2024) 14, https://doi.org/10.1186/s40902-024-00425-w.

[10] N. Mardas, N. Macbeth, N. Donos, R.E. Jung, A.N. Zuercher, Is alveolar ridge preservation an overtreatment? Periodontology 93 (2023) 289–308, https://doi.org/10.1111/prd.12508, 2000.

[11] X. Li, S. Li, H. Qi, D. Han, N. Chen, Q. Zhan, Z. Li, J. Zhao, X. Hou, X. Yuan, X. Yang, Early healing of alveolar bone promoted by microRNA-21-loaded nanoparticles combined with Bio-Oss particles, Chem. Eng. J. 401 (2020) 126026, https://doi.org/10.1016/j.cej.2020.126026.

[12] X.-C. Sun, H. Wang, J. Li, D. Zhang, L.-Q. Yin, Y.-F. Yan, X. Ma, H.-F. Xia, Repair of alveolar cleft bone defects by bone collagen particles combined with human umbilical cord mesenchymal stem cells in rabbit, Biomed. Eng. Online 19 (2020) 1–19, https://doi.org/10.1186/s12938-020-00800-4.

[13] T. Sano, R. Kuraji, Y. Miyashita, K. Yano, D. Kawanabe, Y. Numabe, Biomaterials for alveolar ridge preservation as a preoperative procedure for implant treatment: history and current evidence, Bioengineering 10 (2023) 1376, https://doi.org/10.3390/bioengineering10121376.

[14] G. Funda, S. Taschieri, G.A. Bruno, E. Grecchi, S. Paolo, D. Girolamo, M. Del Fabbro, Nanotechnology scaffolds for alveolar bone regeneration, Materials 13 (2020) 201, https://doi.org/10.3390/ma13010201.

[15] P. Lohmann, A. Willuweit, A.T. Neffe, S. Geisler, T.P. Gebauer, S. Beer, H. H. Coenen, H. Fischer, B. Hermanns-Sachweh, A. Lendlein, N.J. Shah, F. Kiessling, K.-J. Langen, Bone regeneration induced by a 3D architectured hydrogel in a rat critical-size calvarial defect, Biomaterials 113 (2017) 158–169, https://doi.org/10.1016/j.biomaterials.2016.10.039.

[16] J. Wang, W. Cui, Y. Zhao, L. Lei, H. Li, Clinical and radiographic evaluation of Bio-Oss granules and Bio-Oss Collagen in the treatment of periodontal intrabony defects: a retrospective cohort study, J. Appl. Oral Sci. 32 (2024) e20230268, https://doi.org/10.1590/1678-7757-2023-0268.

[17] W. Yao, Z. Song, X. Ma, Y. Huang, X. Zhang, Y. Li, P. Wei, J. Zhang, C. Xiong, S. Yang, Y. Xu, W. Jing, B. Zhao, X. Zhang, Y. Han, Asymmetric adhesive SIS-based wound dressings for therapeutically targeting wound repair, J. Nanobiotechnol. 22 (2024) 34, https://doi.org/10.1186/s12951-024-02294-x.

[18] M. Fujii, R. Tanaka, Porcine small intestinal submucosa alters the biochemical properties of wound healing: a narrative review, Biomedicines 10 (2022) 2213, https://doi.org/10.3390/biomedicines10092213.

[19] Y. Zhao, H. Peng, L. Sun, J. Tong, C. Cui, Z. Bai, J. Yan, D. Qin, Y. Liu, J. Wang, X. Wu, B. Li, The application of small intestinal submucosa in tissue regeneration, Materials Today Bio 26 (2024) 101032, https://doi.org/10.1016/j.mtbio.2024.101032.

[20] Y. Wang, Y. Li, Y. Chen, X. Huang, D. Zuo, X. Tian, Y. Li, W. Wang, Insight into the self-assembly process, microrheological properties and microstructure of acid-soluble collagen from lamb skin under different environmental conditions, Food Biosci. 61 (2024) 104978, https://doi.org/10.1016/j.fbio.2024.104978.

[21] H. Liu, H. Zhang, K. Wang, L. Qi, Y. Guo, C. Zhang, Y. Xu, Impact of ultrasonication on the self-assembly behavior and gel properties of bovine bone collagen I, Molecules 28 (2023) 3096, https://doi.org/10.3390/molecules28073096.

[22] K. Kim, M.S. Kim, An injectable hydrogel derived from small intestine submucosa as a stem cell carrier, J. Biomed. Mater. Res. B Appl. Biomater. 104 (2016) 1544–1550, https://doi.org/10.1002/jbm.b.33504.

[23] Z. Song, H. Yu, L. Hou, Y. Dong, M. Hu, P. Wei, W. Wang, D. Qian, S. Cao, Z. Zheng, Z. Xu, B. Zhao, Y. Huang, W. Jing, X. Zhang, Mechanics-resilient HA/SIS-based composite scaffolds with ROS-scavenging and bacteria-resistant capacity to address infected bone regeneration, Adv. Funct. Mater. 34 (2024) 2315382, https://doi.org/10.1002/adfm.202315382.

[24] Y. Sun, Y. Wang, C. Ji, J. Ma, B. He, The impact of hydroxyapatite crystal structures and protein interactions on bone's mechanical properties, Sci. Rep. 14 (2024) 9786, https://doi.org/10.1038/s41598-024-60701-7.

[25] A. Szcześ, L. Hołysz, E. Chibowski, Synthesis of hydroxyapatite for biomedical applications, Adv. Colloid Interface Sci. 249 (2017) 321–330, https://doi.org/10.1016/j.cis.2017.04.007.

[26] C. Zhen, Y. Shi, W. Wang, G. Zhou, H. Li, G. Lin, F. Wang, B. Tang, X. Li, Advancements in gradient bone scaffolds: enhancing bone regeneration in the treatment of various bone disorders, Biofabrication 16 (2024) 032004, https://doi.org/10.1088/1758-5090/ad4595.

[27] J. Lyu, H. Chen, J. Luo, S. Lin, G. Yang, M. Zhou, J. Tao, Shape memory and hemostatic silk-laponite scaffold for alveolar bone regeneration after tooth extraction trauma, Int. J. Biol. Macromol. 260 (2024) 129454, https://doi.org/10.1016/j.ijbiomac.2024.129454.

[28] M.J. Dewey, A.V. Nosatov, K. Subedi, R. Shah, A. Jakus, B.A.C. Harley, Inclusion of a 3D-printed Hyperelastic Bone mesh improves mechanical and osteogenic performance of a mineralized collagen scaffold, Acta Biomater. 121 (2021) 224–236, https://doi.org/10.1016/j.actbio.2020.11.028.

[29] G. Tozzi, A. De Mori, A. Oliveira, M. Roldo, Composite hydrogels for bone regeneration, Materials 9 (2016) 267, https://doi.org/10.3390/ma9040267.

[30] T. Sun, C. Meng, Q. Ding, K. Yu, X. Zhang, W. Zhang, W. Tian, Q. Zhang, X. Guo, B. Wu, Z. Xiong, In situ bone regeneration with sequential delivery of aptamer and BMP2 from an ECM-based scaffold fabricated by cryogenic free-form extrusion, Bioact. Mater. 6 (2021) 4163–4175, https://doi.org/10.1016/j.bioactmat.2021.04.013.

[31] J. Mondal, S. Pillarisetti, V. Junnuthula, M. Saha, S.R. Hwang, I. Park, Y. Lee, Hybrid exosomes, exosome-like nanovesicles and engineered exosomes for therapeutic applications, J. Contr. Release 353 (2023) 1127–1149, https://doi.org/10.1016/j.jconrel.2022.12.027.

[32] E. Marbán, The secret life of exosomes: what bees can teach us about next-generation therapeutics, J. Am. Coll. Cardiol. 71 (2018) 193–200, https://doi.org/10.1016/j.jacc.2017.11.013.

[33] M. Gao, W. Gao, J.M. Papadimitriou, C. Zhang, J. Gao, M. Zheng, Exosomes—the enigmatic regulators of bone homeostasis, Bone Res 6 (2018) 1–13, https://doi.org/10.1038/s41413-018-0039-2.

[34] J. Huber, M.F. Griffin, M.T. Longaker, N. Quarto, Exosomes: a tool for bone tissue engineering, Tissue Eng. B Rev. 28 (2022) 101–113, https://doi.org/10.1089/ten.teb.2020.0246.

[35] L. Zhang, G. Jiao, S. Ren, X. Zhang, C. Li, W. Wu, H. Wang, H. Liu, H. Zhou, Y. Chen, Exosomes from bone marrow mesenchymal stem cells enhance fracture healing through the promotion of osteogenesis and angiogenesis in a rat model of nonunion, Stem Cell Res. Ther. 11 (2020) 38, https://doi.org/10.1186/s13287-020-1562-9.

[36] X. Han, M. Sun, B. Chen, Q. Saiding, J. Zhang, H. Song, L. Deng, P. Wang, W. Gong, W. Cui, Lotus seedpod-inspired internal vascularized 3D printed scaffold for bone tissue repair, Bioact. Mater. 6 (2021) 1639–1652, https://doi.org/10.1016/j.bioactmat.2020.11.019.

[37] X. Zhang, Y. Xia, J. Xu, J. Kang, X. Li, Y. Li, W. Yan, F. Tian, B. Zhao, B. Li, C. Wang, L. Wang, Cell-free chitosan/silk fibroin/bioactive glass scaffolds with radial pore for in situ inductive regeneration of critical-size bone defects, Carbohydr. Polym. 332 (2024) 121945, https://doi.org/10.1016/j.carbpol.2024.121945.

[38] J. Sun, Z. Yin, X. Wang, J. Su, Exosome-laden hydrogels: a novel cell-free strategy for in-situ bone tissue regeneration, Front. Bioeng. Biotechnol. 10 (2022), https://doi.org/10.3389/fbioe.2022.866208.

[39] L. Sedghi, V. DiMassa, A. Harrington, S.V. Lynch, Y.L. Kapila, The oral microbiome: role of key organisms and complex networks in oral health and disease, Periodontology 87 (2021) 107–131, https://doi.org/10.1111/prd.12393, 2000.

[40] W. Li, H. Liang, X. Lin, T. Hu, Z. Wu, W. He, M. Wang, J. Zhang, Z. Jie, X. Jin, X. Xu, J. Wang, H. Yang, W. Zhang, K. Kristiansen, L. Xiao, Y. Zou, A catalog of bacterial reference genomes from cultivated human oral bacteria, Npj Biofilms Microbiomes 9 (2023) 1–13, https://doi.org/10.1038/s41522-023-00414-3.

[41] B. Lin, R. Li, T.N.G. Handley, J.D. Wade, W. Li, N.M. O'Brien-Simpson, Cationic antimicrobial peptides are leading the way to combat oropathogenic infections, ACS Infect. Dis. 7 (2021) 2959–2970, https://doi.org/10.1021/acsinfecdis.1c00424.

[42] J. Yuan, J. Wang, X. Li, Y. Zhang, J. Xian, C. Wang, J. Zhang, C. Wu, Amphiphilic small molecule antimicrobials: from cationic antimicrobial peptides (CAMPs) to mechanism-related, structurally-diverse antimicrobials, Eur. J. Med. Chem. 262 (2023) 115896, https://doi.org/10.1016/j.ejmech.2023.115896.

[43] L. Zhou, Y. Xing, Y. Ou, J. Ding, Y. Han, D. Lin, J. Chen, Prolonged release of an antimicrobial peptide GL13K-loaded thermosensitive hydrogel on a titanium surface improves its antibacterial and anti-inflammatory properties, RSC Adv. 13 (2023) 23308–23319, https://doi.org/10.1039/D3RA03414C.

[44] F. Jia, D. Xu, Y. Sun, W. Jiang, H. Yang, A. Bian, Y. Liu, K. Liu, S. Zhang, Y. Wang, H. Qiao, H. Lin, J. Lan, Y. Huang, Strontium-calcium doped titanium dioxide nanotubes loaded with GL13K for promotion of antibacterial activity, anti-Inflammation, and vascularized bone regeneration, Ceram. Int. 49 (2023) 35703–35721, https://doi.org/10.1016/j.ceramint.2023.08.250.

[45] K.V. Holmberg, M. Abdolhosseini, Y. Li, X. Chen, S.-U. Gorr, C. Aparicio, Bio-inspired stable antimicrobial peptide coatings for dental applications, Acta Biomater. 9 (2013) 8224–8231, https://doi.org/10.1016/j.actbio.2013.06.017.

[46] T. Li, N. Wang, S. Chen, R. Lu, H. Li, Z. Zhang, Antibacterial activity and cytocompatibility of an implant coating consisting of TiO2 nanotubes combined with a gl13K antimicrobial peptide, IJN 12 (2017) 2995–3007, https://doi.org/10.2147/IJN.S128775.

[47] L. Zhou, Y. Han, J. Ding, X. Chen, S. Huang, X. Xing, D. Wu, J. Chen, Regulation of an antimicrobial peptide GL13K-modified titanium surface on osteogenesis, osteoclastogenesis, and angiogenesis base on osteoimmunology(5), ACS Biomater. Sci. Eng. 7 (2021) 4569–4580, https://doi.org/10.1021/acsbiomaterials.1c00639.

[48] F. Tan, X. Li, Z. Wang, J. Li, K. Shahzad, J. Zheng, Clinical applications of stem cell-derived exosomes, Signal Transduct. Targeted Ther. 9 (2024) 17, https://doi.org/10.1038/s41392-023-01704-0.

[49] D. Wang, H. Cao, W. Hua, L. Gao, Y. Yuan, X. Zhou, Z. Zeng, Mesenchymal stem cell-derived extracellular vesicles for bone defect repair, Membranes 12 (2022) 716, https://doi.org/10.3390/membranes12070716.

[50] T. Wang, Y. Zhou, W. Zhang, Y. Xue, Z. Xiao, Y. Zhou, X. Peng, Exosomes and exosome composite scaffolds in periodontal tissue engineering, Front. Bioeng. Biotechnol. 11 (2024), https://doi.org/10.3389/fbioe.2023.1287714.

[51] F. Khazaei, L. Rezakhani, M. Alizadeh, E. Mahdavian, M. Khazaei, Exosomes and exosome-loaded scaffolds: characterization and application in modern regenerative medicine, Tissue Cell 80 (2023) 102007, https://doi.org/10.1016/j.tice.2022.102007.

[52] H. Chahsetareh, F. Yazdian, M. Pezeshki-Modaress, M. Aleemardani, S. Hassanzadeh, R. Najafi, S. Simorgh, V. Taghdiri Nooshabadi, Z. Bagher, S. M. Davachi, Alginate hydrogel-PCL/gelatin nanofibers composite scaffold containing mesenchymal stem cells-derived exosomes sustain release for regeneration of tympanic membrane perforation, Int. J. Biol. Macromol. 262 (2024) 130141, https://doi.org/10.1016/j.ijbiomac.2024.130141.

[53] W. Lu, M. Zeng, W. Liu, T. Ma, X. Fan, H. Li, Y. Wang, H. Wang, Y. Hu, J. Xie, Human urine-derived stem cell exosomes delivered via injectable GelMA templated hydrogel accelerate bone regeneration, Materials Today Bio 19 (2023) 100569, https://doi.org/10.1016/j.mtbio.2023.100569.

[54] P. Guan, C. Liu, D. Xie, S. Mao, Y. Ji, Y. Lin, Z. Chen, Q. Wang, L. Fan, Y. Sun, Exosome-loaded extracellular matrix-mimic hydrogel with anti-inflammatory property Facilitates/promotes growth plate injury repair, Bioact. Mater. 10 (2022) 145–158, https://doi.org/10.1016/j.bioactmat.2021.09.010.

[55] S. Ma, J. Wu, H. Hu, Y. Mu, L. Zhang, Y. Zhao, X. Bian, W. Jing, P. Wei, B. Zhao, J. Deng, Z. Liu, Novel fusion peptides deliver exosomes to modify injectable thermo-sensitive hydrogels for bone regeneration, Materials Today Bio 13 (2022) 100195, https://doi.org/10.1016/j.mtbio.2021.100195.

[56] Y. Ji, J. Zhou, T. Sun, K. Tang, Z. Xiong, Z. Ren, S. Yao, K. Chen, F. Yang, F. Zhu, X. Guo, Diverse preparation methods for small intestinal submucosa (SIS): decellularization, components, and structure, J. Biomed. Mater. Res. 107 (2019) 689–697, https://doi.org/10.1002/jbm.a.36582.

[57] D.J.S. Hulmes, Collagen Diversity, Synthesis and Assembly, (n.d.).

[58] S.H. Zaky, K.W. Lee, J. Gao, A. Jensen, K. Verdelis, Y. Wang, A.J. Almarza, C. Sfeir, Poly (glycerol sebacate) elastomer supports bone regeneration by its mechanical properties being closer to osteoid tissue rather than to mature bone, Acta Biomater. 54 (2017) 95–106, https://doi.org/10.1016/j.actbio.2017.01.053.

[59] Q. Hu, M. Liu, G. Chen, Z. Xu, Y. Lv, Demineralized bone scaffolds with tunable matrix stiffness for efficient bone integration, ACS Appl. Mater. Interfaces 10 (2018) 27669–27680, https://doi.org/10.1021/acsami.8b08668.

[60] M. Chen, F. Zhao, Y. Li, M. Wang, X. Chen, B. Lei, 3D-printed photoluminescent bioactive scaffolds with biomimetic elastomeric surface for enhanced bone tissue engineering, Mater. Sci. Eng. C 106 (2020) 110153, https://doi.org/10.1016/j.msec.2019.110153.

[61] J.H. Wen, L.G. Vincent, A. Fuhrmann, Y.S. Choi, K.C. Hribar, H. Taylor-Weiner, S. Chen, A.J. Engler, Interplay of matrix stiffness and protein tethering in stem cell differentiation, Nat. Mater. 13 (2014) 979–987, https://doi.org/10.1038/nmat4051.

[62] H. Mohammadi, M. Sepantafar, N. Muhamad, A. Bakar Sulong, How does scaffold porosity conduct bone tissue regeneration? Adv. Eng. Mater. 23 (2021) 2100463 https://doi.org/10.1002/adem.202100463.

[63] Y. Zhang, N. Sun, M. Zhu, Q. Qiu, P. Zhao, C. Zheng, Q. Bai, Q. Zeng, T. Lu, The contribution of pore size and porosity of 3D printed porous titanium scaffolds to osteogenesis, Biomater. Adv. 133 (2022) 112651, https://doi.org/10.1016/j.msec.2022.112651.

[64] Y. Liu, Y. Sun, S. Li, M. Liu, X. Qin, X. Chen, Y. Lin, Tetrahedral framework nucleic acids deliver antimicrobial peptides with improved effects and less susceptibility to bacterial degradation(10), Nano Lett. 20 (2020) 3602–3610, https://doi.org/10.1021/acs.nanolett.0c00529.

[65] X. Zhang, W. Wang, J. Chen, M. Lai, Peptide GL13K releasing hydrogel functionalized micro/nanostructured titanium enhances its osteogenic and antibacterial activity, J. Biomater. Sci. Polym. Ed. 34 (2023) 1036–1052, https://doi.org/10.1080/09205063.2022.2155780.

[66] Y. Mu, S. Ma, P. Wei, Y. Wang, W. Jing, Y. Zhao, L. Zhang, J. Wu, B. Zhao, J. Deng, Z. Liu, Multifunctional modification of SIS membrane with chimeric peptides to promote its antibacterial, osteogenic, and healing-promoting abilities for applying to GBR, Adv. Funct. Mater. 31 (2021) 2101452, https://doi.org/10.1002/adfm.202101452.

[67] J. Dai, N.G. Fischer, J.R. Rahimi, H. Wang, C. Hu, W. Chen, Y. Lin, T. Sang, H. P. Chew, L. Kong, C. Aparicio, Z. Ye, S. Huang, Interpenetrating nanofibrillar membrane of self-assembled collagen and antimicrobial peptides for enhanced bone regeneration, Int. J. Biol. Macromol. 267 (2024) 131480, https://doi.org/10.1016/j.ijbiomac.2024.131480.

[68] S. Zhang, S.J. Chuah, R.C. Lai, J.H.P. Hui, S.K. Lim, W.S. Toh, MSC exosomes mediate cartilage repair by enhancing proliferation, attenuating apoptosis and modulating immune reactivity, Biomaterials 156 (2018) 16–27, https://doi.org/10.1016/j.biomaterials.2017.11.028.

[69] Z. Song, W. Yao, X. Zhang, Y. Dong, Z. Zhang, Y. Huang, W. Jing, L. Sun, Y. Han, F. Hu, Z. Yuan, B. Zhao, P. Wei, X. Zhang, Controlled growth of metal-organic frameworks on small intestinal submucosa for wound repair through combined antibacterial and angiogenic effects, Nano Today 54 (2024) 102060, https://doi.org/10.1016/j.nantod.2023.102060.

[70] M. Li, C. Zhang, M. Cheng, Q. Gu, J. Zhao, Small intestinal submucosa: a potential osteoconductive and osteoinductive biomaterial for bone tissue engineering, Mater. Sci. Eng. C 75 (2017) 149–156, https://doi.org/10.1016/j.msec.2017.02.042.

[71] E.-J. Lee, M. Jain, S. Alimperti, Bone microvasculature: stimulus for tissue function and regeneration, Tissue Eng. B Rev. 27 (2021) 313–329, https://doi.org/10.1089/ten.teb.2020.0154.

[72] C. Mahapatra, P. Kumar, M.K. Paul, A. Kumar, Angiogenic stimulation strategies in bone tissue regeneration, Tissue Cell 79 (2022) 101908, https://doi.org/10.1016/j.tice.2022.101908.

[73] F. Diomede, G.D. Marconi, L. Fonticoli, J. Pizzicanella, I. Merciaro, P. Bramanti, E. Mazzon, O. Trubiani, Functional relationship between osteogenesis and angiogenesis in tissue regeneration, Int. J. Mol. Sci. 21 (2020) 3242, https://doi.org/10.3390/ijms21093242.

[74] S. Pan, Z. Yin, C. Shi, H. Xiu, G. Wu, Y. Heng, Z. Zhu, J. Zhang, J. Gui, Z. Yu, B. Liang, Multifunctional injectable hydrogel microparticles loaded with miR-29a abundant BMSCs derived exosomes enhanced bone regeneration by regulating osteogenesis and angiogenesis, Small 20 (2024) 2306721, https://doi.org/10.1002/smll.202306721.

[75] G. De Souza Balbinot, V.C.B. Leitune, E.A. Da Cunha Bahlis, D. Ponzoni, F. Visioli, F.M. Collares, Niobium-containing bioactive glasses modulate alkaline phosphatase activity during bone repair, J. Biomed. Mater. Res. 111 (2023) 1224–1231, https://doi.org/10.1002/jbm.b.35227.

[76] M. Ou, X. Huang, Influence of bone formation by composite scaffolds with different proportions of hydroxyapatite and collagen, Dent. Mater. 37 (2021) e231–e244, https://doi.org/10.1016/j.dental.2020.12.006.

[77] B. Lowe, J.G. Hardy, L.J. Walsh, Optimizing nanohydroxyapatite nanocomposites for bone tissue engineering, ACS Omega 5 (2020) 1–9, https://doi.org/10.1021/acsomega.9b02917.

[78] D. Wang, H. Cao, W. Hua, L. Gao, Y. Yuan, X. Zhou, Z. Zeng, Mesenchymal stem cell-derived extracellular vesicles for bone defect repair, Membranes 12 (2022) 716, https://doi.org/10.3390/membranes12070716.

[79] G. Lu, P. Cheng, T. Liu, Z. Wang, BMSC-derived exosomal miR-29a promotes angiogenesis and osteogenesis, Front. Cell Dev. Biol. 8 (2020). https://www.frontiersin.org/articles/10.3389/fcell.2020.608521. (Accessed 14 February 2023).

[80] S. Ma, Y. Zhao, Y. Yang, Y. Mu, L. Zhang, J. Wu, R. Li, X. Bian, P. Wei, W. Jing, B. Zhao, Z. Liu, J. Deng, Asymmetric SIS membranes specifically loaded with exosomes through the modification of engineered recombinant peptides for guide bone regeneration, Compos. B Eng. 232 (2022) 109571, https://doi.org/10.1016/j.compositesb.2021.109571.

[81] L. Liu, S. Guo, W. Shi, Q. Liu, F. Huo, Y. Wu, W. Tian, Bone marrow mesenchymal stem cell-derived small extracellular vesicles promote periodontal regeneration, Tissue Eng. 27 (2021) 962–976, https://doi.org/10.1089/ten.tea.2020.0141.

[82] S. Alghamdi, Isolation and identification of the oral bacteria and their characterization for bacteriocin production in the oral cavity, Saudi J. Biol. Sci. 29 (2022) 318–323, https://doi.org/10.1016/j.sjbs.2021.08.096.

[83] K.A. Berry, M.T.A. Verhoef, A.C. Leonard, G. Cox, Staphylococcus aureus adhesion to the host, Ann. N. Y. Acad. Sci. 1515 (2022) 75–96, https://doi.org/10.1111/nyas.14807.

[84] L. Qin, N. Hu, Y. Zhang, J. Yang, L. Zhao, X. Zhang, Y. Yang, J. Zhang, Y. Zou, K. Wei, C. Zhao, Y. Li, H. Zeng, W. Huang, Q. Zou, Antibody-antibiotic conjugate targeted therapy for orthopedic implant-associated intracellular S. aureus infections, J. Adv. Res. (2023), https://doi.org/10.1016/j.jare.2023.12.001.

[85] A. Mulukutla, R. Shreshtha, V. Kumar Deb, P. Chatterjee, U. Jain, N. Chauhan, Recent advances in antimicrobial peptide-based therapy, Bioorg. Chem. 145 (2024) 107151, https://doi.org/10.1016/j.bioorg.2024.107151.

[86] C. Qi, Q. Sun, D. Xiao, M. Zhang, S. Gao, B. Guo, Y. Lin, Tetrahedral framework nucleic acids/hyaluronic acid-methacrylic anhydride hybrid hydrogel with antimicrobial and anti-inflammatory properties for infected wound healing, Int. J. Oral Sci. 16 (2024) 30, https://doi.org/10.1038/s41368-024-00290-3.

[87] M. Hassanpour, A.A. Salybekov, S. Kobayashi, T. Asahara, CD34 positive cells as endothelial progenitor cells in biology and medicine, Front. Cell Dev. Biol. 11 (2023), https://doi.org/10.3389/fcell.2023.1128134.

[88] T. Komori, Functions of osteocalcin in bone, pancreas, testis, and muscle, Int. J. Mol. Sci. 21 (2020) 7513, https://doi.org/10.3390/ijms21207513.

[89] A. Zheng, X. Wang, X. Xin, L. Peng, T. Su, L. Cao, X. Jiang, Promoting lacunar bone regeneration with an injectable hydrogel adaptive to the microenvironment, Bioact. Mater. 21 (2023) 403–421, https://doi.org/10.1016/j.bioactmat.2022.08.031.

[90] U.H. Lerner, C. Ohlsson, The WNT system: background and its role in bone, J. Intern. Med. 277 (2015) 630–649. https://doi.org/10.1111/joim.12368.

[91] S. Miao, J. Zhou, B. Liu, X. Lei, T. Wang, X. Hao, P. Cheng, H. Wu, Y. Song, G. Pei, L. Bi, A 3D bioprinted nano-laponite hydrogel construct promotes osteogenesis by activating PI3K/AKT signaling pathway, Materials Today Bio 16 (2022) 100342, https://doi.org/10.1016/j.mtbio.2022.100342.

[92] Z. Hao, L. Ren, Z. Zhang, Z. Yang, S. Wu, G. Liu, B. Cheng, J. Wu, J. Xia, A multifunctional neuromodulation platform utilizing Schwann cell-derived exosomes orchestrates bone microenvironment via immunomodulation,

angiogenesis and osteogenesis, Bioact. Mater. 23 (2023) 206–222, https://doi.org/10.1016/j.bioactmat.2022.10.018.

[93] M. Yin, Z. Liu, Z. Sun, X. Qu, Z. Chen, Y. Diao, Y. Cheng, S. Shen, X. Wang, Z. Cai, B. Lu, S. Tan, Y. Wang, X. Zhao, F. Chen, Biomimetic Scaffolds Regulating the Iron Homeostasis for Remolding Infected Osteogenic Microenvironment, Advanced Science n/a (n.d.) 2407251. https://doi.org/10.1002/advs.202407251.

[94] Q. Li, H. Yu, M. Sun, P. Yang, X. Hu, Y. Ao, J. Cheng, The tissue origin effect of extracellular vesicles on cartilage and bone regeneration, Acta Biomater. 125 (2021) 253–266, https://doi.org/10.1016/j.actbio.2021.02.039.

[95] J. Zhang, X. Liu, H. Li, C. Chen, B. Hu, X. Niu, Q. Li, B. Zhao, Z. Xie, Y. Wang, Exosomes/tricalcium phosphate combination scaffolds can enhance bone regeneration by activating the PI3K/Akt signaling pathway, Stem Cell Res. Ther. 7 (2016) 136, https://doi.org/10.1186/s13287-016-0391-3.

[96] M. Wu, S. Wu, W. Chen, Y.-P. Li, The roles and regulatory mechanisms of TGF-β and BMP signaling in bone and cartilage development, homeostasis and disease, Cell Res. 34 (2024) 101–123, https://doi.org/10.1038/s41422-023-00918-9.